Atmospheric CO_2 estimates for the Miocene to Pleistocene based on foraminiferal $\delta^{11}B$ at Ocean Drilling Program Sites 806 and 807 in the Western Equatorial Pacific

Maxence Guillermic[1,2], Sambuddha Misra[3,4], Robert Eagle[1,2], Aradhna Tripati[1,2]

[1]Department of Atmospheric and Oceanic Sciences, Department of Earth, Planetary, and Space Sciences, Center for Diverse Leadership in Science, Institute of the Environment and Sustainability, University of California – Los Angeles, Los Angeles, CA 90095 USA

[2]Laboratoire Géosciences Océan UMR6538, UBO, Institut Universitaire Européen de la Mer, Rue Dumont d'Urville, 29280, Plouzané, France

[3] Indian Institute of Science, Centre for Earth Sciences, Bengaluru, Karnataka 560012, India

[4] The Godwin Laboratory for Palaeoclimate Research, Department of Earth Sciences, University of Cambridge, UK

Correspondence to: Maxence Guillermic (maxence.guillermic@gmail.com) and Aradhna Tripati (atripati@g.ucla.edu)

ABSTRACT

Constraints on the evolution of atmospheric CO_2 levels throughout Earth's history are foundational to our understanding of past variations in climate. Despite considerable effort, records vary in their temporal and spatial coverage and estimates of past CO_2 levels do not always converge, and therefore new records and proxies are valuable. Here we reconstruct atmospheric CO_2 values across major climate transitions over the past 16 million years using the boron isotopic composition ($\delta^{11}B$) of planktic foraminifera from 89 samples obtained from two sites in the West Pacific Warm Pool, Ocean Drilling Program (ODP) Sites 806 and 807 measured using high-precision multi-collector inductively-coupled plasma mass spectrometry. We compare our results to published data from ODP Site 872, also in the Western Equatorial Pacific, that goes back to 22 million years ago. These sites are in a region that today is near equilibrium with the atmosphere and are thought to have been in equilibrium with the atmosphere for the interval studied. We show that $\delta^{11}B$ data from this region are consistent with other boron-based studies. The data show evidence for elevated pCO_2 during the Middle Miocene and Early to Middle Pliocene, and reductions in pCO_2 of ~200 ppm during the Middle Miocene Climate Transition, ~250 ppm during Pliocene Glacial Intensification, and ~50 ppm during the Mid-Pleistocene Climate Transition. During the Mid-Pleistocene Transition there is a minimum pCO_2 at MIS 30. Our results are consistent with a coupling between pCO_2, temperature and ice sheet expansion from the Miocene to Recent.

Highlights

In this study, we reconstruct atmospheric pCO_2 using $\delta^{11}B$ data from ODP Sites 806 and 807 and compare them with ice core data. We therefore apply the same framework to older samples to create a long-term pH and pCO_2 reconstruction for the past 16 million years, and recalculate pCO_2 for ODP Site 872 from 17 to 22 million years ago. We find major increases in surface water pH and decreases in atmospheric pCO_2 were associated with decreased temperature in the Western Equatorial Pacific, including associated with major episodes of ice sheet expansion in the high latitudes, providing more robust quantitative constraints on the past coupling between pCO_2, temperature, and cryosphere stability.

Keywords

Boron isotopes, CO_2, ODP Site 806, ODP Site 807, Miocene, climate

1. Introduction

Due to concerns about the long-term consequences of anthropogenic emissions and associated climate change (IPCC, 2014, 2018), efforts have been made to quantify past atmospheric CO_2 and examine past relationships between CO_2 and temperature. Such data are not only critical for constraining Earth-system sensitivity (Lea, 2004; Lunt et al., 2010; Pagani et al., 2010; Hansen et al., 2012, 2013, Foster and Rohling, 2013; Schmittner et al., 2011; Tierney et al., 2020), but are also of broad interest to contextualize the evolution of climate and geological systems through Earth's history (Tripati et al., 2011; Foster et al., 2017; Tripati and Darby, 2018). However, discrepancies between proxy reconstructions still exist, including for major climate transitions of the Cenozoic. In particular, there remains a pressing need for robust and higher-resolution atmospheric CO_2 records from regions that are in equilibrium with the atmosphere.

High-resolution and direct determinations of atmospheric CO_2 are available for the last 800 kyr through analysis of air bubbles extracted from ice-cores, but these records are limited to the availability of cores (Petit et al., 1999; Siegenthaler et al., 2005; Lüthi et al., 2008; Bereiter et al., 2015). A window into atmospheric CO_2 levels comes from 1 million-year-old blue ice (Higgins et al., 2015) and from a second snapshot from 1.5 Ma (Yan et al., 2019). Most reconstructions of CO_2 for prior to 800 ka are based on indirect terrestrial and marine proxies. Stomata indices for fossil leaves (Van der Burgh, 1993; Royer , 2001), carbon isotope ratios ($\delta^{13}C$) of paleosols (Retallak et al., 2009), $\delta^{13}C$ of alkenones (Pagani et al., 2005; Zhang et al., 2013), B/Ca ratios of surface-dwelling foraminifera (Yu and Hönisch, 2007; Foster, 2008; Tripati et al., 2009, 2011), and boron isotope ratios ($\delta^{11}B$) of surface-dwelling foraminifera (e.g. Pearson and Palmer., 2000; Hönisch and Hemming, 2009; Seki et al., 2010; Bartoli et al., 2011; Foster, 2008, 2012; Badger et al., 2013; Foster and Sexton, 2014; Greenop et al., 2014; Martinez-Boti et al., 2015a; Chalk et al., 2017; Sosdian et al., 2018; Dyez et al., 2018; deLaVega et al., 2020; Greenop et al., 2021; Rae et al., 2021; Raitzsch et al., 2021; Shuttleworth et al., 2021) have been used to estimate atmospheric CO_2.

Each of the above proxy methods has sources of systematic errors that we do not attempt to exhaustively document as they have been discussed in-depth elsewhere (e.g., Pagani et al., 2005; Tripati et al., 2011; Guillermic et al., 2020). However, we note that significant developments in the boron-based proxies include improvements to the accuracy and precision of measurements using multi-collector inductively coupled mass spectrometry (MC-ICP-MS) compared to early work with negative thermal ionization mass spectrometry (N-TIMS), where there were large instrumental mass fractionations and challenges with laboratory intercomparison (Foster et al., 2013; Farmer et al., 2016; Aggarwal and You, 2017). There was also the realization that temperature-dependent K_D to interpreting B/Ca sensitivities observed from the field of sediment trap, core-top, and downcore studies (Yu and Hönisch, 2007; Foster et al., 2008; Tripati et al., 2009, 2011; Babila et al., 2010; Osborne et al., 2020) differ from foraminiferal culture experiments (Allen et al., 2011, 2012) and

inorganic calcite (Mavromatis et al., 2015); this type of discrepancy has also been observed with other elemental proxies (e.g., Mg/Ca). Such differences may be due to differences in growth rates (Sadekov et al., 2014), ontogenetic changes, a correlation in the field between temperature and other hydrographic variables that obscure robust statistical determination of parameter relationships, culture conditions resulting in organisms being stressed, and/or other factors.

The marine CO_2 proxy that appears to be subject to the fewest systematic uncertainties, based on our current understanding, is the boron isotopic composition ($\delta^{11}B$) of planktic foraminifera as measured using MC-ICP-MS and N-TIMS (Hain et al., 2018). This proxy provides constraints on seawater pH, if temperature, salinity, seawater $\delta^{11}B$, and the appropriate mono-specific calibration between $\delta^{11}B_{carbonate}$ and $\delta^{11}B_{borate}$ are constrained (Pearson and Palmer, 2000; Foster et al., 2008; Sosdian et al., 2018; Raitzsch et al., 2018; Guillermic et al., 2020). Seawater pH can be used to calculate seawater pCO_2 if there are constraints on a second parameter of the carbonate system (e.g. alkalinity, DIC). Atmospheric pCO_2 can then be constrained if the site being examined is in air-sea CO_2 equilibrium or if the disequilibrium is known and stable through time.

However, there are relatively few studies generating high-precision boron-based records over major climate transitions in the Cenozoic using recent analytical methods and that incorporate our current understanding of the proxy (e.g., Greenop et al., 2014; Martinez-Boti et al., 2015b; Chalk et al., 2017; Dyez et al., 2018; Sosdian et al., 2018; de la Vega et al., 2020; Rae et al., 2021; Raitzsch et al., 2021). Furthermore, of the existing studies using boron-based proxies, an additional uncertainty frequently exists, namely the short time interval of study (e.g., emphasizing on a climate transition) (Martinez-Boti et al., 2015b; Chalk et al., 2017) and whether the study sites remain in air-sea CO_2 equilibrium with the atmosphere (Martinez et al., 2015a). And although estimation of atmospheric pCO_2 from seawater pH using this proxy is relatively straightforward, reconstructions are still impacted by uncertainties including the lack of robust constraints on a second parameter of the carbonate system, and our limited understanding of secular variations in the $\delta^{11}B$ of seawater (Tripati et al., 2011; Greenop et al., 2017; Sosdian et al., 2018; Rae et al., 2021).

Therefore, to provide additional constraints on the evolution of atmospheric pCO_2 from the Miocene through Pleistocene, we developed new records from the western tropical Pacific. We use foraminiferal $\delta^{11}B$ and trace elements in the planktic foraminiferal species *Trilobus sacculifer* and *Globigerinoides ruber* to reconstruct past seawater pH and atmospheric CO_2 at Ocean Drilling Program (ODP) Sites 806 and 807 in the Western Equatorial Pacific (WEP) over the last 16 million years (Myr). The sites are located on the western border of the tropical Pacific Ocean, the largest open-oceanic region on the globe, and the warmest open ocean region at present.

These two sites have been examined in other boron-based studies (Wara et al., 2003; Tripati et al., 2009, 2011; Shankle et al., 2020), as has the region more broadly (Pearson and Palmer, 2000; Sosdian et al., 2018), because it is understood to be in equilibrium with the atmosphere and have

relative stable hydrography. The region experiences equatorial divergence but is not strongly affected by upwelling and has a current estimated annual air-sea CO_2 difference of +28 ppmv (Takahashi et al., 2014). The pre-industrial air-sea CO_2 difference is calculated to be +16 ppm, (GLODAP database corrected from anthropogenic inputs), with a value of 298 ppm, compared to the ice core value of 282 ppm at 1.08 ka . This pCO_2 difference is similar to our pCO_2 uncertainty (an average of ~17 ppm (2 SD) for the youngest samples). If trade winds were much stronger, and equatorial divergence greater, than this could drive some disequilibrium in the past. However, a few lines of evidence suggest the region was in quasi-equilibrium in the past: 1) zonal temperatures are at a maximum in pre-industrial times and during the Pleistocene, and we are able to reconstruct atmospheric pCO_2 values from the ice cores, 2) temperature proxies indicate the region is relatively stable with respect to temperature compared to other parts of the ocean, and also indicate a weak and stable zonal temperature gradient during the Miocene and Pliocene which would support air-sea stable conditions and air-sea equilibrium (e.g., Nathan and Leckie, 2009; Zhang et al. 2014; Liu et al., 2019).

Thus, this study builds on low-resolution prior reconstructions for these sites (Wara et al., 2003; Tripati et al., 2009, 2011; Shankle et al., 2020), Site 872 in the tropical Pacific (Sosdian et al., 2018), and other published boron isotope work, to provide additional data to constrain past seawater pH and pCO_2 for the WEP using MC-ICP-MS, thereby providing a new perspective on reconstructing past atmospheric CO_2 via marine sediment archives. We explore various constraints on the second carbonate system parameter using a number of different scenarios, following on the systematic work done by Tripati et al. (2009) and (2011) for B/Ca. We interpret these data using recent constraints on seawater $\delta^{11}B$ (Lemarchand et al., 2000; Raitzsch and Hönisch, 2013; Greenop et al., 2017). For temperature estimation, we utilize a multi-variable model for Mg/Ca correcting from salinity, pH and seawater Mg/Ca (Gray and Evans, 2019), that builds on prior work with clumped isotopes in planktic foraminifera for Site 806 and other WEP sites demonstrating that for the Last Glacial Maximum to recent, salinity-corrected Mg/Ca values are needed to yield convergent estimates of mixed-layer temperatures (Tripati et al., 2014).

2. Materials and Methods

Below we describe site locations, analytical methods used, and principal figures. The supplemental methods section describes screening for potential contamination, equations used for calculations, and error propagation.

2.1 Site locations

Samples are from three ODP holes recovered during Leg 130 in the WEP (Fig. 1, Table 1): Hole 806A (0°19.140'N, 159°21.660'E, 2520.7 m water depth), Hole 806B (0°19.110'N, 159°21.660'E, 2519.9 m water depth), and Hole 807A (3°36.420'N, 156°37.500'E, 2803.8 m water

158 depth) (Berger et al., 1993). Sites 806 and 807 are not likely to have experienced major tectonic
159 changes over the last 20 million years.
160
161 **2.2 Preservation**
162 Microfossils in sediments at these sites, as with any sedimentary sequences, have the potential
163 to be influenced by diagenesis. Despite evidence of authigenic carbonate formation, recent modeling
164 work concluded the influence of dissolution and reprecipitation at Sites 806 and 807 was relatively
165 minor (Mitnik et al., 2018). Prior work has also found minimal impacts on the B/Ca ratio of Pliocene
166 foraminifera from Site 806 (White and Ravelo, 2020), and on the Mg/Ca ratio of Miocene *D. altispera*
167 shells at Site 806 (Sosdian et al., 2020). The weight/shell ratio is commonly used to monitor
168 dissolution, and the only published record at Site 806 for the Pliocene does not show a trend
169 consistent with dissolution of *T. sacculifer* (Wara et al., 2005). We do note that while the "coccolith
170 size-free dissolution" index reported in Si and Rosenthal (2019) indicates higher dissolution rates in
171 the Miocene, their records were thought to be biased from changes in foraminifera assemblages as
172 discussed in White and Ravelo (2020).
173 To further assess the potential impact of dissolution in our geochemical data, the weight/shell
174 ratio was examined in our samples. The weight/shell data used to monitor dissolution does not exhibit
175 any trend within the interval studied consistent with dissolution. Absolute weights/shell are increasing
176 in the Miocene, which is not consistent with dissolution influencing the record (Fig. 2E).
177 Additionally, reconstructed pH and pCO_2 values also exhibit reasonable correspondence with the ice
178 core data. Downcore $\delta^{11}B$ values from Sites 806 and 807 are similar, despite evidence for higher
179 authigenic carbonate at Site 807 relative to Site 806 (Mitnik et al., 2018). Further, despite different
180 sedimentation rates, our $\delta^{11}B$ and Mg/Ca results are consistent between Sites 806 and 807 , and with
181 data from Site 872 (Sosdian et al., 2018), which implies that diagenesis is not a primary driver of the
182 reconstructed trends. Comparison of raw data, and derived parameters, is shown in Figs. 2 and 7.
183
184 **2.3 Age models**
185 The age model for Site 806 from 0-1.35 Ma is based on Medina-Elizalde and Lea (2005);
186 calculated ages correspond well with ages from the Lisiecki and Raymo LR04 stack (Fig. 2A). The
187 fourth polynomial regression-based biostratigraphy from Lear et al. (2015) was used for the rest of the
188 record, following other work (Sosdian et al., 2020). Ages for Site 807 are based on published
189 biostratigraphy (Berger et al., 1993) with additional constraints placed by Zhang et al. (2007) for the
190 interval from 0-0.55 Ma. Benthic $\delta^{18}O$ values from Sites 806 and 807 show good correspondence for
191 the last 0.55 Myr, and the low-resolution benthic $\delta^{18}O$ record for Site 806 (Lear et al., 2003; 2015) is
192 consistent with the stack from Lisiecki and Raymo, (2005) for the period studied (Fig. 3).
193

2.4 Species and trace element cleaning

Samples were picked and cleaned to remove clays at UCLA (Los Angeles, CA) and the University of Western Brittany (Plouzané, France). 50-100 foraminifera shells were picked from the 300-400µm fraction size for *T. sacculifer* (w/o sacc) and from the 250-300 µm for *G. ruber* (white sensu stricto). Picked foraminifera were gently crushed, clays removed, and checked for coarse-grained silicates. Samples were then cleaned using a full reductive and oxidative cleaning protocol following Barker et al. (2003). A final leach step with 0.001N HCl was done prior dissolution in 1N HCl. Boron purification used a published microdistillation protocol (see Misra et al., 2014b, Guillermic et al., 2020 for more detailed methods).

2.5 Chemical purification and geochemical analysis

Chemical separation was performed in a boron-free clean lab at the University of Cambridge (Cambridge, UK). Calcium concentrations were measured on an ICP-AES ®Ultima 2 HORIBA at the Pôle Spectrometrie Océan (PSO), UMR6538 (Plouzané, France). Elemental ratios (e.g. X/Ca ratios) were analyzed on a Thermo Scientific ®Element XR HR-ICP-MS at the PSO, Ifremer (Plouzané, France). Boron isotopic measurements were carried out on a Thermo Scientific ®Neptune+ MC-ICP-MS equipped with 10^{13} Ohm resistor amplifiers (Lloyd et al., 2018) at the University of Cambridge (Cambridge, UK).

2.6 Standards

Variations in B isotope ratios are expressed in conventional delta (δ) notation with $\delta^{11}B$ values reported against the reference standard NIST SRM 951 (NIST, Gaithersburg, MD, USA):

$$\delta^{11}B\ (‰) = 1000 \times \left(\frac{^{11}B/^{10}B_{Sample}}{^{11}B/^{10}B_{NIST\ SRM\ 951}} - 1\right) \qquad \textbf{eq. 1}$$

Multiple analyses of external standards were performed to ensure data quality. For boron isotopic measurements, JC_P-1 (Geological Survey of Japan, Tsukuba, Japan, Gutjahr et al., 2020) was used as a carbonate standard, and NEP, a *Porites sp* coral from University of Western Australia and Australian National University was also used (McCulloch et al., 2014). A boron isotope liquid standard, ERM© AE121 (certified $\delta^{11}B = 19.9 \pm 0.6$ ‰, SD), was used to monitor reproducibility and drift during each session (Vogl and Rosner, 2012; Foster et al., 2013; Misra et al., 2014b). For trace elements, external reproducibility was determined using the consistency standard Cam-Wuellerstorfi (University of Cambridge) (Misra et al., 2014b).

2.7 Figures of Merit

2.7.1 $\delta^{11}B$ analyses

Samples measured for boron isotopes typically ranged in concentration from 10 ppb B (~5ng B) to 20 ppb B samples (~10ng B). Sensitivity was 10mV/ppb B (eg. 100mV for 10ppb B) in wet plasma at 50µl/min sample aspiration rate. The intensity of ^{11}B for a sample at 10 ppb B was typically 104 ± 15 mV (2 SD, typical session) and closely matched the 98 ± 6 mV (2 SD, typical session) of the standard. Procedural boron blanks ranged from 15 pg B to 65 pg B (contributed to less than 1 % of the sample signal). The acid blank during analyses was measured at ≤ 1mV on the ^{11}B (which also is < 1 % of the sample intensity), and no memory effect was seen within and across sessions.

External reproducibility was determined by analyzing the international standard JC_{P}-1 (Gutjahr et al., 2020) and a *Porites sp.* coral (NEP). The boron isotopic composition of JC_{P}-1 was measured at 24.06 ± 0.20 ‰ (2 SD, n=6) within error of published values of 24.37 ± 0.32 ‰, 24.11± 0.43 ‰ and 24.42 ± 0.28 ‰ from Holcomb et al. (2015), Farmer et al. (2016) and Sutton et al. (2018), respectively. Average values are $\delta^{11}B_{NEP}$ = 25.72 ± 0.79 ‰ (2 SD, n=31) determined over 13 different analytical sessions, with each number representing a separately processed sample from this study. These results are within error of published values of 26.20 ± 0.88 ‰ (2 SD, n = 27) and 25.80 ± 0.89 ‰ (2 SD, n = 6), from Holcomb et al. (2015) and Sutton et al. (2018), respectively. Data are reported in Supplementary Table B.

2.7.2 X/Ca analyses

Trace element (TE) analyses were conducted at a Ca concentration of either 10 or 30 ppm. Typical blanks for a 30 ppm Ca session were: ^{7}Li < 2 %, ^{11}B < 7 %, ^{25}Mg < 0.2 % and ^{43}Ca < 0.02 %. Additionally, blanks for a 10 ppm Ca session were: ^{7}Li < 2.5 %, ^{11}B < 10 %, ^{25}Mg < 0.4 % and ^{43}Ca < 0.05 %. Analytical uncertainty of a single measurement was calculated from the reproducibility of the CamWuellestorfi standard: 0.6 µmol/mol for Li/Ca, 8 µmol/mol for B/Ca and 0.02 mmol/mol for Mg/Ca (2 SD, n=48). Data are reported in Supplementary Table B.

2.8 Calculations

Detailed calculations can be found in the supplemental materials. Briefly, Mg/Ca was used to reconstruct sea surface temperature (SST) using the framework from Gray and Evans. (2019) correcting for influences of pH, salinity, and secular variation in seawater Mg/Ca. $\delta^{11}B_{carbonate}$ was corrected using an empirical $\delta^{11}B_{carbonate}$-weight/shell ratio relationship. $\delta^{11}B_{borate}$ was determined using species dependent sensitivities of $\delta^{11}B_{carbonate}$ to $\delta^{11}B_{borate}$ (Guillermic et al., 2020). pH was calculated using the $\delta^{11}B_{borate}$ with different scenarios of secular seawater $\delta^{11}B$ changes (Lemarchand et al., 2002; Raitzsch and Hönisch, 2013; Greenop et al., 2017). pCO_2 was reconstructed using pH based

261 $\delta^{11}B_{carbonate}$ and different scenarios of alkalinity (Tyrell and Zeebe, 2004; Ridgwell and Zeebe, 2005;
262 Caves et al. 2016 and Rae et al. 2021). Further details including equations are in the Supplement.
263
264 **3. Results and discussion**
265 **3.1 Geochemical results**
266 Geochemical data used in this study are presented in Figure 2. Mg/Ca data (Fig. 2C) are
267 consistent with previously published Mg/Ca values for Site 806 on *T. sacculifer* (Wara et al., 2005;
268 Tripati et al., 2009; Nathan and Leckie, 2009). Although the record we generated does not overlap
269 with Site 872, they are 1 myr apart (15.7 and 16.7 Ma); there is a good correspondence between our
270 Mg/Ca data and the published Mg/Ca record from *T. trilobus* at Site 872 (Sosdian et al., 2018). Mg/Ca
271 from a different species, *D. altispira* (Sosdian et al., 2020), is also plotted with an offset, for
272 comparison.
273 Comparison with Site 872 data that is part of the compilation from Sosdian et al. (2018)
274 shows that their $\delta^{11}B$ data are in line with our dataset (Figure 2B), and all sites examined in the WEP
275 (Sites 806, 807, and 872) are above the lysocline (Kroenke et al. 1991). The $\delta^{11}B$ data for *T. sacculifer*
276 exhibit a significant decrease (4.2 ‰) from the Miocene to present. Figure 2B also compares the $\delta^{11}B$
277 data used in this study with published data from other sites and shows that raw $\delta^{11}B$ data for the WEP
278 can be lower than values for other regions.
279
280 **3.2 Reproducing pCO_2 from ice cores**
281 We sought to assess if there is evidence for air-sea equilibrium or disequilibrium in the WEP
282 during the large amplitude late Pleistocene glacial/interglacial cycles, in order to validate our
283 approach. We reconstructed pCO_2 for the last 800 kyr (n=16, Fig. 3). For the last 800 kyr,
284 reconstructed pCO_2 values for Sites 806 and 807 are in the range from ice cores (Fig. 3, Petit et al.,
285 1999, Siegenthaler et al., 2005, Lüthi et al., 2008; compilation from Bereiter et al., 2015). The two
286 critical diagnostics we used for method validation are: 1) that the $\delta^{11}B$-based reconstruction of pCO_2
287 is consistent with ice core atmospheric CO_2 and 2) the boron-based reconstruction empirically
288 reproduces interglacial-glacial amplitudes from ice cores. Fig. 3B shows that both of these criteria are
289 met. We also created a crossplot comparing these two independent constraints on pCO_2 (Fig. 3C).
290 Two regressions between ice core pCO_2 and boron-based pCO_2 are shown, with a simple linear
291 regression (grey line) and a Deming regression that factors in error in variables (blue line), and
292 bootstraps of outputs shown (n=1000, Figure 3C, Table S6). While slopes and intercepts are not
293 statistically different from a 1:1 line, the regressions do not reach a high significance level (p=0.25);
294 boosting the resolution of the record could help provide better constraints for this type of comparison.
295 The age models for the site do not provide an explanation for this variability based on comparison of
296 the benthic $\delta^{18}O$ records for both Sites 806 and 807 (Fig. 3A, Zhang et al., 2007; Lear et al., 2003;

297 Lear et al., 2015) to the published isotopic stack (Lisiecki and Raymo, 2004). No significant
298 difference in variability was observed at either site. We also note that reconstructed pCO_2
299 uncertainties (both accuracy and precision) could potentially arise from Mg/Ca-derived estimates of
300 temperature; these uncertainties could be reduced using independent temperature proxies for the WEP
301 such as clumped isotope thermometry (Tripati et al., 2010; 2014), a technique that is not sensitive to
302 the same sources of error as Mg/Ca thermometry, and therefore is an area planned for future work.
303 Other sources of uncertainty that have a larger effect on pCO_2 calculations are the weight/shell
304 correction, while the TA and seawater boron isotope composition have a minor effect over this time
305 interval.
306 Between MIS 7 and 6, our reconstructions exhibit a decrease in temperature (ΔT) of 1.2 °C,
307 an increase in pH (ΔpH) of 0.08 and a decrease in pCO_2 (ΔpCO_2) of 58 ppm. Between stage 3 and 1,
308 we observed an increase of temperature of 2.0 °C, a decrease of pH of 0.13 and an increase in pCO_2 of
309 76 ppm. We also compare results with recent reconstructions in Figs. S1 and S2 (Sosdian et al., 2018;
310 Rae et al., 2021). These results highlight that we are able to reproduce the range of atmospheric pCO_2
311 in the ice core record, and reproduce the amplitude of changes between transitions, with uncertainties
312 typical for this type of work (Hönisch et al., 2019).
313
314 **3.3 Sea surface temperature in the WEP**
315 Mg/Ca data are consistent at Site 806 (Wara et al., 2005; Tripati et al., 2009, 2011; Nathan
316 and Leckie, 2009) and Site 872 (Sosdian et al., 2018) in the WEP. The Mg/Ca in *T. sacculifer* has to
317 date not shown a pH dependency (Gray and Evans, 2019) but Mg/Ca of *G. ruber* does and was
318 therefore corrected from this effect (see supplemental material). Data for both species were corrected
319 from salinity and seawater Mg/Ca changes. Mg/Ca-temperatures for Site 872 was reconstructed using
320 published data and the same framework we use here and are presented in Figure 4. Recalculated
321 values for Site 872 are from *D. altispera*, with an offset applied relative to *T. sacculifer*, and show
322 similar variations to our record for the MCO-MMCT periods (Sosdian et al., 2020). Temperatures
323 from Tex_{86} and $U^{K'}_{37}$ are plotted for comparison but those records are limited to the last 12 and 5 Myrs
324 respectively (Zhang et al., 2014).
325 The Mg/Ca data support high temperatures of 35.2 ± 1.3 °C (2SD, n=11) for the early
326 Miocene until the MMCT, with relatively small (ca. 1°C) change from into the MCO, and larger
327 changes out of the MCO. Similarly warm SST for the MCO were reconstructed in the North Atlantic
328 at Site 608 from Tex_{86} (Super et al., 2018). Despite a gap in our compilation from 11.5 to 9.5 Ma,
329 there is a SST decrease of ~6 °C from the MCO to ~7 Ma where temperatures similar to present day
330 values are observed. A decline in temperature during the MMCT is coincident with the timing of a
331 constriction of the Indonesian Seaway, the pre-closure of the trans-equatorial circulation and
332 subsequent formation of a proto-warm pool (Nathan and Leckie, 2009; Sosdian et al., 2020). From 12

to 7 Ma, the Mg/Ca-SST record diverges from Tex_{86} and $U^{K'}_{37}$-based reconstructions, with higher temperatures. At the same time, a record for the North Atlantic showed a decrease of ~10 °C from the MCO to ~9 Ma (Super et al., 2018). From 7 Ma to present, the record from multiple proxies – Mg/Ca, Tex_{86}, and $U^{K'}_{37}$, in the WEP agree.

3.4 Scenarios of seawater $\delta^{11}B$ and alkalinity used for pCO_2 reconstructions

Figures 5 and 6 show the different histories of seawater $\delta^{11}B$ and alkalinity used for calculations, respectively. Details of calculations are in the Supplemental methods. Following the approach of Tripati et al. (2009, 2014) and recent literature (Sosdian et al., 2018; Rae et al., 2021), we explored multiple scenarios for the evolution of seawater boron geochemistry (Fig. 5) and alkalinity for calculations of pCO_2 (Figs. 6, S1 and S2). During the interval overlapping with the ice core record, we observe that the choice of model used does not make a significant difference in reconstructed values. During earlier time intervals, we see there is a greater divergence, reflecting larger uncertainties in seawater $\delta^{11}B$ and alkalinity further back in Earth history.

Prior to 10 Ma and during the early Pliocene (~4.5 to 3.5 Ma), calculations of pCO_2 diverge from published values largely because of the different assumptions each study has used for past seawater $\delta^{11}B$ (Fig. 5). However, we find that when the uncertainty in reconstructed pH is fully propagated, the differences in reconstructed pH values calculated using each of the $\delta^{11}B_{seawater}$ histories is not significantly different (Fig. 5 and 6; see also Hönisch et al., 2019). In contrast to the results from Greenop et al. (2017), the record from Raitzsch and Hönisch, (2013) exhibits substantial variations on shorter timescales. Such variability is a challenge to reconcile with the Li isotope record of Misra and Froelich, (2012), given that Li has a shorter residence time than boron while having similar sources and sinks. For the remainder of this study, we use the $\delta^{11}B_{seawater}$ history from Greenop et al. (2017) because it is in good agreement with seawater $\delta^{7}Li$ (Misra and Froelich, 2012). The recent calculations of seawater pH (Sosdian et al., 2018; Rae et al., 2021) agree with values from our study when uncertainties are taking into account (Fig. 5).

The four alkalinity models used in this study diverge prior to 9 Ma, with a maximum difference at ~13 Ma that is also reflected in reconstructed pCO_2 values (Fig. 6). However, all four models yield pCO_2 estimates that are within error of each other when the full uncertainty is considered. Uncertainty in the evolution of seawater alkalinity and seawater $\delta^{11}B$ leads to differences in the absolute values of pCO_2 reconstructed (Fig. S2), and a divergence in pCO_2 values reconstructed that is largest in the Miocene. The two scenarios that produce the highest divergence in values are those calculated using constant alkalinity relative to those calculated using values from McCaves et al. (2016), with a maximum difference at 15.06 Ma of up to 250 ppm CO_2, and with the latter model producing lower values (Figs. 6B and 6E). Thus, for the MCO, alkalinity is a critical parameter in calculations of absolute pCO_2 values. For the Miocene and earlier intervals, improved constraints on

past secular variations of seawater $\delta^{11}B$ and alkalinity will yield more accurate reconstructions of pCO_2.

For the remainder of this paper, we use the model of Caves et al. (2016) to estimate alkalinity and $\delta^{11}B_{seawater}$ determined by Greenop et al. (2017) (e.g. Fig. 6E). We note that two recent syntheses of boron isotope data have been published and compare our results to these findings (Figs. 8 and S2). Sosdian et al. (2018) reports values that are in line with our results in the Miocene but their study does not replicate results from ice cores. Rae et al. (2021) presents reconstructed values that are higher in the Miocene, due to the utilization of different scenarios of seawater $\delta^{11}B$ and alkalinity compared to this work.

3.5 Time intervals

3.5.1 Miocene

The study of Miocene climate is thought to provide a useful analog for changes associated with global warming and melting of polar ice, in concert with ocean circulation (Holbourn et al., 2013). The Miocene epoch (23-5.3 Ma) is characterized by a warm interval, the Miocene Climate Optimum (~17-14.7 Ma - MCO), and an abrupt cooling during the Middle Miocene Climate Transition (~14-13 Ma – MMCT) that led to the expansion of ice on Antarctica and Greenland. Climate modeling supports a role for decreasing CO_2 in this transition (DeConto and Pollard, 2003). However, reconstructions for the Miocene are still relatively limited (Sosdian et al., 2018; Rae et al., 2021; Raitzsch et al., 2021). Boron isotope and alkenone-based pCO_2 reconstructions support higher pCO_2 during the MCO and a decrease over the MMCT (Sosdian et al. 2018; Stoll et al., 2019), consistent with what was previously inferred from B/Ca (Tripati et al., 2009, 2011; Sosdian et al., 2020).

We applied the same framework we used for calculations at Sites 806 and 807 to published boron isotope data from Site 872 (Sosdian et al., 2018) in order to extend the WEP record to the early Miocene (Figs. 7, 8). The Miocene data between Sites 806 and 872 do not overlap as both are low in resolution, but do show excellent correspondence in their trends in $\delta^{11}B$ and reconstructed pH. For example, the closest datapoints in time at the two sites are at 15.6 Ma at Site 806 with a $\delta^{11}B = 14.47 \pm 0.21$ ‰, and at 16.7 Ma at Site 872, with a $\delta^{11}B = 15.12 \pm 0.25$ ‰. The pH values we reconstruct are within error of published estimates from Site 872 (Sosdian et al. 2018, Figs. 7D and 8D). Collectively, these data suggest the early Miocene WEP was characterized by a mixed-layer pH of 8.1 ± 0.1 (2 SD, n=4) between 19.4 and 21.8 Ma, which decreased to reach a minimum during the MCO of 7.7 ($\pm^{0.11}_{0.14}$).

Given the sensitivity in absolute pCO_2 to assumptions about the second carbonate system parameter, a few scenarios were explored for the combined 806/807/872 reconstructed pH values. For all alkalinity scenarios we used, reconstructed pCO_2 shows an increase from the Early Miocene to the MCO, with the highest values in the MCO. Recalculated pCO_2 for Site 872 between 19.4 and 21.8 Ma

is 232 ± 92 ppm (2 SD, n=4), lower but within error of the ones presented in Sosdian et al. (2018) and also within error of a constant alkalinity scenario (Fig 8D). The main difference between our calculations and published reconstructions occurs between 19.4 and 21.8 Ma, when the same $\delta^{11}B$ data for Site 872 from Sosdian et al. (2018) recalculated in Rae et al. (2021) yield higher pCO_2, with an average value of 591 ± 238 ppm (2 SD, n=4) because of the different assumptions used in their calculations. This difference is important because the assumptions from Rae et al. (2021) would imply a relatively high and stable pCO_2 from the early Miocene to MCO (Fig. S2), which would imply a decoupling between pCO_2 and temperature with no pCO_2 change during an interval of decreasing benthic $\delta^{18}O$. However, our reconstructed pCO_2 increase towards the MCO is in line with the observed benthic $\delta^{18}O$ decrease and $\delta^{13}C$ increase and suggest a coupling between temperature and pCO_2 over this period. This highlights the critical need for the use of a common set of assumptions for studies. Assumptions may vary between studies depending of the timescales studied, but a common framework is needed. In addition, further constraints on the second carbonate system parameter and on secular changes in seawater $\delta^{11}B$ will reduce uncertainties in reconstructed pCO_2, with improved precision.

The highest pCO_2 values we reconstruct are during the MCO (Fig. 6E). For the MCO, our estimates are 511 ± 201 ppm (2 SD, n=3, Table 2). The middle Miocene values we reconstruct are in line with previous studies (Greenop et al., 2014; Sosdian et al., 2018). Published $\delta^{11}B$-based reconstructions also support higher pCO_2 for the MCO of ~350-400 ppm (Foster et al., 2012) or 300-500 ppm (Greenop et al., 2014) that was recalculated by Sosdian et al. (2018) to be ~470-630 ppm depending on the model of $\delta^{11}B_{seawater}$ chosen. During the MCO relative maxima in pCO_2, our data support very warm sea surface temperatures in the WEP (35.6 ± 0.6 °C 2SD, n=3; Fig. 8C), that merits further examination in future studies. In fact, the highest temperatures recorded in our samples occur when there is a minimum in the global composite record of $\delta^{18}O$ of benthic foraminifera (Zachos et al., 2001, 2008; Tripati and Darby, 2018).

At the end of the MMCT, we find evidence for changes in pCO_2 and temperature in the WEP (Fig. 8). From 13.5 to 12.7 Ma, we reconstruct an increase of pH ~0.21 and a major decrease of pCO_2 of ~215 ppm during an interval highlighted by Flower and Kennett, (1996), who observed changes in $\delta^{18}O$ indicative of rapid East Antarctic Ice Sheet growth and enhanced organic carbon burial with a maximum $\delta^{13}C$ reached at ~13.6 Ma (Shevenell et al., 2004; Holbourn et al., 2007). As discussed in section 3.4 the alkalinity model used for the calculations have an important impact during the Miocene which is likely responsible for the different absolute pCO_2 values over the MCO. In comparison, a scenario of constant alkalinity would lead to a pCO_2 during the MCO of 714 ± 313 ppm (2 SD, n=3) and a decrease of ~540 ppm during the MMCT. Both those reconstructions could simulate the large-scale advance and retreat of Antarctic ice with such low pCO_2 values (Gasson et al., 2016). At the same time, we find evidence for a decline in SST of 3.4 °C to minimum values of 33.3

°C. The synchronous shifts in the $\delta^{13}C$ and $\delta^{18}O$ of benthic foraminifera are consistent with increased carbon burial during colder periods, thus feeding back into decreasing atmospheric CO_2, and supporting the hypothesis that the drawdown of atmospheric CO_2 can in part, be explained by enhanced export of organic carbon (Flower and Kennett, 1993, 1996). However, given the limited sampling of this study, we are only able to resolve a pCO_2 decrease toward the end of the MMCT (~13.5 Ma). The higher resolution $\delta^{11}B$-pCO_2 from Site 1092 for the MMCT (Raitzsch et al. 2021) reports eccentricity-scale pCO_2 variability; the authors reported that low pCO_2 during eccentricity maxima was consistent with an increase in weathering due to strengthened monsoonal circulation, which would increase nutrient delivery and supporting higher productivity that in turn would impact carbon drawdown and burial, in line with modeling from Ma et al. (2011).

The resolution of our data during the late Miocene is low, with a data gap from 12.5 to 9.2 Ma, and another gap between 6.5 and 5 Ma. We note the pCO_2 peak at ~9 Ma observed by Sosdian et al. (2018) is not seen in our record although this is likely due to the low resolution of our dataset. Between 9.5 and 7.1 Ma we find evidence for a decrease in atmospheric CO_2 of 100 ppm associated with a decrease in temperature of 1.3 °C. pCO_2 estimates derived from alkenones for Site 1088 (Tanner et al., 2020) do not show the same trend as boron-based reconstructions from the WEP or other regions (Figure 6), which might be due to other controls on the alkenone proxy (Badger et al., 2019). A recent publication from Raitzsch et al. (2021) reports a $\delta^{11}B$ reconstruction of pCO_2 that is within error of other $\delta^{11}B$ isotope data from the Southern Ocean (Sosdian et al., 2018), although not for the same period as Tanner et al. (2020). pCO_2 differences between our reconstruction and that of Sosdian et al. (2018) and Raitzcsh et al. (2021) (Fig. 8) likely reflect assumptions made for calculations (of $\delta^{11}B$, TA) and the specific mono-specific calibrations used for each study, as well as potential geographic differences in air-sea pCO_2. These differences do not invalidate the boron isotope proxy but illustrate the impact that specific seawater parameters and calibrations can have on reconstructed pCO_2 values, as well as potential inferences of air-sea disequilibrium.

3.5.2 Pliocene

Oxygen isotope data from a global benthic foraminiferal stack show that the Pliocene epoch (5.3-2.6 Ma) was initially characterized by warm conditions followed by the intensification of glaciation that occurred in several steps, including during MIS M2 (3.312-3.264 Ma), followed by the Middle Pliocene Warm Period (Lisiecki and Raymo, 2005). The Middle Pliocene Warm Period (mPWP – 3.29-2.97 Ma) is considered a relevant geological analogue for future climate change given ~3°C warmer global temperatures and sea levels that were ~20 m higher than today (Dutton et al., 2015; Haywood et al., 2016), and is a target for model intercomparison projects, for which accurate paleo-atmospheric pCO_2 estimates are critical (Haywood et al., 2016).

We calculate high pCO_2 values of 419 ± 119 ppm (2 SD, n=3, Table 2) between 4.7 to 4.5 Ma

during the Early Pliocene warm interval (Figure 9). The pCO_2 data we report provide a higher data density for the Early Pliocene, and exhibit a trend that is in line with the reconstruction from Rae et al. (2021). Our data support values of 530 ± 110 ppm over the mPWP (2 SD, n = 4), higher than previously published data (Figs. 9, S2 and Table 2), although we acknowledge our low data density may not fully sample variability over this period. The similarity between our reconstructed values and those published for Site 871 in the Indian Ocean (Sosdian et al., 2018) suggests that changes in Indonesian through-flow do not induce substantial changes in air-sea exchange in the WEP.

The warmth and local pCO_2 maxima of the mPWP (mid-Pliocene Warm Period) was followed by a strong decrease of temperature in upwelling and high latitude regions during from 3.3-2.7 Ma, coincident with glacial intensification in the Northern Hemisphere. This climate transition was hypothesized to be driven by the closure of the Panama seaway the opening of the high latitudes and subsequent modifications of oceanic circulation (Haug and Tiedemann, 1998). However, modeling from Lunt et al. (2008) supports an additional major role for CO_2 in the glaciation. pCO_2 thresholds have been proposed to explain the intensification of Northern Hemisphere Glaciation, with values proposed ranging from 280 ppm (DeConto et al., 2008) to 200 to 400 ppm (Koening et al., 2011).

The pCO_2 concentrations that we calculate indicates a reduction to 350 ppm by 2.7 Ma, ~280 ppm by 2.6 Ma, and ~210 ppm by 2.4 Ma, in several steps. These results support roughly a halving of CO_2 values when compared to values of ~530 ppm at 3.3 Ma. These values are consistent with the pCO_2 thresholds proposed by both DeConto et al. (2008) and Koening et al. (2011) for the intensification of Northern Hemisphere glaciation and the low atmospheric CO_2 (280 ppmv) scenario from Lunt et al. (2008). Mg/Ca SST decline from 30°C to 26°C, supporting an Earth System sensitivity of ~4°C/doubling of CO_2 over this range, although given uncertainties, higher values of ~6°C/doubling of CO_2 that have recently been proposed (Tierney et al., 2020) can not be excluded.

We speculate that associated with Pliocene glacial intensification, at 4.42, 3.45 and 2.67 Ma, it is possible that the declines in CO_2 and ice growth in turn drove substantial changes in pole-to-equator temperature gradients and winds, that in turn may have impacted iron cycling (Watson et al., 2000; Robinson et al., 2005; Martinez-Garcia et al., 2011), stratification (Toggweiler, 1999; Sigman et al., 2010), and other feedbacks that impact the amplitude of glacial/interglacial cycles and have been implicated as factors that could have contributed to Pliocene glacial intensification. Specifically, as the mean climate state of the planet became cooler, and glacial-interglacial cycles became larger in amplitude, enhanced windiness and dust transport and upwelling during glacials (Martinez-Boti et al., 2015b) may have enhanced iron fertilization and subsequent carbon export (Martinez-Garcia et al., 2011). While data resolution are limited, we speculate this could explain why glacial/interglacial amplitudes in WEP pCO_2 values decrease from the mPWP towards the Pleistocene, whereas variations in $\delta^{18}O$ are increasing – a speculation that could be tested with increased data resolution.

513

514 **3.5.3 Pleistocene**

515 During the Pleistocene (2.58-0.01 Ma), the climate system experienced a transition in
516 glacial/interglacial (G/I) variability from low amplitude, higher frequency and obliquity-dominated
517 oscillations (i.e., ~ 41 kyr) of the late Pliocene to the high amplitude, lower frequency and
518 eccentricity-dominated cycles (i.e, ~100 kyr) of the last 800 kyr. This transition is termed the Middle
519 Pleistocene Transition (1.2-0.8 Ma – MPT). Questions have been raised about the role of atmospheric
520 CO_2 during this transition, including using boron-based proxies (Hönisch et al., 2009; Tripati et al.,
521 2011; Chalk et al., 2017). Previous boron isotope studies for ODP Sites 668 and 999 in the tropical
522 Atlantic Ocean have suggested that a decline in atmospheric CO_2 did occur during glacial periods in
523 the MPT, but not during interglacials (Hönisch et al., 2009; Chalk et al., 2017; Dyez et al., 2018).

524 Our pCO_2 concentrations for Sites 806/807 reported here are in good agreement with those
525 determined from ice cores from the early Pleistocene (Yan et al., 2019, Figs. 9 and 10), and with the
526 boron-derived pCO_2 from a recent compilation (Rae et al., 2021). Results for the MPT are broadly in
527 the range of values reported by Hönisch et al. (2009) and Chalk et al. (2017). Although our data are
528 relatively limited, we note they have greater resolution for the middle and later part of the transition
529 than prior publications that have drawn conclusions about the MPT (Hönisch et al., 2009; Chalk et al.,
530 2017; Dyez et al., 2018) (Fig. 10D) and therefore we explore their implications.

531 Taken alone, or when combined with the published data from Chalk et al. (2017) (that is also
532 based on MC-ICPMS), our results support a possible reduction of both glacial and interglacial pCO_2
533 values. We also find evidence that during the MPT, glacial pCO_2 declined rapidly from 189 ±30 ppm
534 at MIS 36 (Chalk et al., 2017) to reach a minimum of 170 ($\pm^{52}_{24}$) ppm during MIS 30. We note that
535 pCO_2 concentrations are within error when uncertainty is fully propagated, and then remained
536 relatively stable until the end of the MPT whereas interglacial pCO_2 values decrease gradually to
537 reach post-MPT values.

538 In our record for the last 16 Myr, the lowest pCO_2 is recorded at MIS 30 during the MPT,
539 with values of 164 ($\pm^{44}_{35}$) ppm, which supports an atmospheric CO_2 threshold that leads to large sheet
540 generation. During this transition, the pCO_2 threshold needed to build sufficiently large ice sheets that
541 were able to survive the critical orbital phase of rising obliquity to ultimately switch to a 100 kyr
542 world, was likely reached at MIS 30, but a higher pCO_2 resolution of the MPT is needed for
543 confirmation. The multiple feedbacks resulting from stable ice sheets (iron
544 fertilization/productivity/changes in albedo/ changes in deep water formation) might have sustained
545 larger mean global ice volumes over the subsequent 800 kyr. An asymmetrical decrease between
546 pCO_2 values during interglacials relative to glacials, with glacials exhibiting the largest change across

the MPT, would have led to increased sequestration of carbon during glacials in the 100 kyr world, as discussed by Chalk et al. (2017), with increased glacial dust input and iron fertilization.

3.6 Changes in volcanic activity and silicate weathering, and long-term pCO_2

On million-year timescales, atmospheric CO_2 is controlled by its input through mantle degassing in the form of sub-aerial and sub-aqueous volcanic activity and its removal by chemical weathering of continental silicate rocks. Over the last 16 Myr, two relative maxima in atmospheric pCO_2 are observed in our record, one during the MCO (at 15.67 Ma) and a second around the late Miocene/early Pliocene (beginning at 4.7 and 4.5 Ma) (Fig. 11), though the timing for the latter is not precise. The strong pCO_2 increase from the early Miocene to MCO is timely with increasing volcanic activity (Foster al. 2012), associated with the eruption of the Columbia River Flood Basalts (Hooper et al., 2002; Kasbohm and Schoene, 2018), with recent geochronologic evidence published supporting higher eruption activity between 16.7 and 15.9 Ma (Kasbohm and Schoene, 2018) reinforcing the idea of an episodic pCO_2 increase during the MCO due to volcanic activity. Underestimation of net CO_2 outgassing from specific continental flood basalt eruption is possible, as both sub-aqueous and sub-aerial flood basalts, under right climatic conditions, are prone to enhanced chemical weathering. For example, the 4-5‰ drop in δ^7Li record at the K-Pg boundary (Misra and Froelich, 2012) is attributed to rapid quasi-congruent weathering of Deccan Traps (Rene et al. 2015) during their eruption. Courtillot and Rene (2003) estimate that about 50% of emitted CO_2, roughly equivalent to the amount emitted by the eruption of a million cubic kilometers of Deccan Traps, may be missing due to chemical and physical weathering. Additionally, the early Eocene (at ~50 Ma) 3-4‰ rise in seawater δ^7Li at a time where there is not significant uplift of the Himalayas (Misra & Froelich, 2012) is also attributed to incongruent weathering of previously erupted Deccan Trap basalts as the Indian subcontinent moved from arid mid-latitudes to the wet low latitudes (Kent and Muttoni, 2008). Thus, a significant part of the outgassed CO_2 can be consumed by chemical weathering of freshly erupted hot basalts (Courtillot et al., 2003). However, the congruency of chemical weathering of basalts, depending on regional climatic conditions (warm-wet vs. cold-arid), will determine the nature of observable inflection in the seawater δ^7Li. The possible quantification of increased rates of silicate weathering inferred from δ^7Li (mentioned below) can be utilized to determine total eruptive volume (missing + existing) and volatile emissions from the Columbia River Flood Basalts. At the same time as continental flood basalt emissions, enhanced seafloor production could also be a second possible source of CO_2; however, we note there is evidence that the rate of seafloor production has remained virtually invariant over the last 60 million years (Rowley, 2002; Muller et al. 2016).

The second CO_2 peak can possibly be caused either by the observed increase in global volcanism during the early/middle Pliocene (Kennett and Thunell, 1977; Kroenke et al., 1993), and/or a by change in silicate weathering regime. Strontium and lithium isotopes ($^{87/86}Sr$ and δ^7Li) have been used as proxy for silicate weathering flux and congruency. Although the strontium isotope record

584 exhibits a monotonous increase, lithium isotope data (Misra and Froelich, 2012) are more variable
585 with a transition from a period of increase seawater δ^7Li (e.g. non-steady state weathering) to stable
586 seawater δ^7Li (e.g., steady state weathering) beginning at roughly 6.8 Ma (Fig. 11).
587 It is interesting to note that the rise in δ^7Li (Fig. 11B) from the early Miocene to the MCO are
588 synchronous with the rise in pCO_2. Before 18.5 Ma, the pCO_2 is relatively stable, δ^7Li is increasing,
589 suggesting non-steady state / incongruent nature of continental chemical weathering. From 18.6 to
590 16.7 Ma, the δ^7Li record decreases by ~2 ‰, consistent with decreasing weathering rates and an
591 associated increase in pCO_2. Between 16.7 and 15.9 Ma, when the eruption of the Columbia River
592 Flood Basalts is at a maximum, δ^7Li increases, in line with higher weathering rates that could arise
593 from higher atmospheric CO_2 and the presence of fresh basalts. The δ^7Li record then decreases again
594 until the end of the MCO at ~14.7 Ma, in line with a decrease in the eruption rate, sustaining high
595 atmospheric CO_2. A constant increase in δ^7Li is then observed, until the early Pliocene, where there is
596 evidence for a shift to a steady-state weathering regime. This increase in δ^7Li is also consistent with
597 the decrease in pCO_2 observed until the early Pliocene.
598
599 **3.9 Conclusions**
600 We developed a reconstruction of atmospheric pCO_2 based on $\delta^{11}B$ of planktic foraminifera
601 from ODP Sites 806 and 807 located in the Western Equatorial Pacific for the past 16 million years
602 and extended the record to 22 Ma by reprocessing data from Site 872 (Sosdian et al., 2018). We build
603 on past efforts to reconstruct atmospheric pCO_2 using different proxies from this region, including
604 from carbon isotopes in marine organic matter (Rayno et al., 1996) and alkenones (Pagani et al.,
605 2010), as well as foraminiferal B/Ca ratios (Tripati et al., 2009, 2011), all of which have been shown
606 to have a number of complexities and potential sources of systematic error (e.g., Tripati et al., 2011).
607 It also builds on efforts using boron isotopes in other regions using MC-ICP-MS (Seki et al., 2010;
608 Foster et al., 2012, 2014; Greenop et al., 2014; Martinez-Boti et al., 2015b; Stap et al., 2016; Chalk et
609 al., 2017; Dyez et al., 2018; de la Vega et al., 2020), and our recent work constraining fractionation
610 factors and measuring small samples of foraminifera (Guillermic et al., 2020).
611 Our study contributes a new long-term reconstruction of atmospheric pCO_2 for the Neogene
612 derived from boron isotopes from the tropical Pacific Ocean. Although the record is not continuous,
613 with variable resolution, it captures both long-term and short-term variability associated with several
614 key transitions and demonstrates the utility of examining sites in the Western Equatorial Pacific for
615 future higher-resolution studies. Results for Sites 806 and 807 in the Western Equatorial Pacific
616 reproduce the amplitude of late Pleistocene glacial-interglacial cycles in pCO_2. These observations are
617 consistent with the sites being in equilibrium with the atmosphere, although further work would be
618 useful to explore sources of uncertainty and differences relative to ice core pCO_2.
619 Values increase from the Miocene to the Miocene Climatic Optimum, and the MCO values
620 for this region has higher pCO_2 than reconstructions from other areas, with values estimated as 511 ±

201 ppm (2 SD, n=3). These elevated values are likely linked to the eruption of the Columbia River Flood Basalts, with values declining into the early Pliocene, including during Pliocene glacial intensification. The changes in pCO_2 we observed are in line with changes in δ^7Li, a proxy of silicate weathering, and future modeling of multiple proxy records should be insightful. Early Pliocene data for ~4.7-4.5 Ma support high pCO_2 of 419 ± 119 ppm, and elevated values during the mid-Pliocene Warm Period of 530 ± 110 ppm for ~3.3-3.0 Ma. These data are low in resolution, thereby not fully sampling orbital and millennial scale variability. The higher resolution record for Pliocene glacial intensification supports a reduction in pCO_2 during several steps, with values at 2.7 Ma of 350 ppm, 2.6 Ma of ~280 ppm, and 2.4 Ma of ~210 ppm. We find support for a larger reduction in glacial pCO_2 during the Mid-Pleistocene Transition compared to interglacial pCO_2, and a minimum in pCO_2 during glacial MIS 30. These findings confirm a role for CO_2 in the transition from a 41 kyr to a 100 kyr world.

Higher-resolution boron isotope records from the WEP would allow for further resolution of these changes. Additional constraints on temperature, such as from clumped isotopes (Tripati et al., 2010) in the WEP (Tripati et al., 2014), could allow for uncertainties in pCO_2 estimates from boron isotopes to be reduced and for new constraints on Earth climate sensitivity. Future constraints on the vertical structure of the tropical Pacific (Shankle et al., 2021) during these transitions may also potentially be illuminating.

Data availability

All data are available in the supplemental materials. Reconstructed climate parameters and proxy data will be archived at the *NOAA's* NCEI World Data Service for Paleoclimatology on acceptance at https://www.ncei.noaa.gov/products/paleoclimatology.

Author Contributions

AT developed the project and wrote the proposals that funded the work. All authors contributed to the experimental design. MG performed the measurements with assistance from SM. MG conducted data analysis with input from AT. MG drafted the paper, which was edited by all authors. Interpretation was led by MG and AT, with input from SM and RE.

Competing interests

The authors declare that they have no conflict of interest.

Acknowledgments

The authors wish to thank the Tripati Lab, including Lea Bonnin and Alexandra Villa, for assistance with picking samples; the IODP core repository for provision of samples; Mervyn Greaves for

technical support and use of laboratory space at the University of Cambridge; Yoan Germain, Emmanuel Ponzevera, Céline Liorzou and Oanez Lebeau for technical support and use of laboratory space at IUEM and Ifremer (Plouzané, France). We thank Thomas Chalk, another anonymous reviewer, and Hubertus Fischer for their helpful comments on the manuscript, and Mathis Hain for discussion of this work.

Financial support

This research is supported by DOE BES grant no. DE-FG02-13ER16402 to AKT, by the International Research Chair Program that is funded by the French government (LabexMer ANR-10-LABX-19-01) to AKT and RAE, and IAGC student research grant 2017.

6. References

Aggarwal, S. K., & You, C. F.: A review on the determination of isotope ratios of boron with mass spectrometry. Mass Spectrometry Reviews, 36(4), 499-519, 2017.

Allen, K. A. and Hönisch, B.: The planktic foraminiferal B/Ca proxy for seawater carbonate chemistry, A critical evaluation, Earth Planet. Sci. Lett, 345–348, 203–211, 2012.

Allen, K. A., Hönisch, B., Eggins, S. M., Yu, J., Spero, H. J., Elderfield, H.: Controls on boron incorporation in cultured tests of the planktic foraminifer Orbulina universa. Earth and Planetary Science Letters, 309(3-4), 291-301, 2011.

Anagnostou, E., John, E. H., Edgar, K. M., Foster, G. L., Ridgwell, A., Inglis, G. N., D. Pancost, R., J. Lunt, D., Pearson, P. N.: Changing atmospheric CO2 concentration was the primary driver of early Cenozoic climate. Nature, 533(7603), 380-384, 2016.

Babila, T., Huang, K. F., Rosenthal, Y., Conte, M. H., & Lin, H. L. Development of B/Ca as a seawater pH proxy using sediment trap time series, abstract, 2010.

Badger M. P. S., Chalk T. B., Foster G. L., Bown P. R., Gibbs S. J., Sexton P. F., Schmidt D. N., Pälike H., Mackensen A. and Pancost R. D.: Insensitivity of alkenone carbon isotopes to atmospheric CO2 at low to moderate CO2 levels. Climate of the Past, 15(2), 539-554, 2019.

Badger M. P. S., Lear C. H., Pancost R. D., Foster G. L., Bailey T. R., Leng M. J. and Abels H. A.: CO2 drawdown following the middle Miocene expansion of the Antarctic Ice Sheet. Paleoceanography 28, 42–53, 2013.

Barker S., Greaves M. and Elderfield H.: A study of cleaning procedures used for foraminiferal Mg/Ca paleothermometry. Geochemistry, Geophys. Geosystems 4, 1–20, 2003.

Bartoli G., Hönisch B. and Zeebe R. E.: Atmospheric CO2 decline during the Pliocene intensification of Northern Hemisphere glaciations. Paleoceanography 26, 1–14, 2011.

Berger, W.H., Kroenke, J.W., Mayer, L.A.: Proceedings of the Ocean Drilling Program, Scientific Results, Vol. 130, 1993.

Berger, W.H., Kroenke, L., Janecek, T.R., et al., . Proceedings of the Ocean Drilling Program. Initial Reports, p. 130, 1991.

Bian, N., & Martin, P. A.: Investigating the fidelity of Mg/Ca and other elemental data from reductively cleaned planktonic foraminifera. Paleoceanography, 25(2), 2010.

Bolton C. T. and Stoll H. M.: Late Miocene threshold response of marine algae to carbon dioxide limitation. Nature 500, 558–562, 2013.

Bolton C. T., Hernández-Sánchez M. T., Fuertes M.-Á., González-Lemos S., Abrevaya L., Mendez-Vicente A., Flores J.-A., Probert I., Giosan L., Johnson J. and Stoll H. M. : Decrease in coccolithophore calcification and CO2 since the middle Miocene. Nat. Commun. 7, 10284, 2016.

Boyer, T.P., J. I. Antonov, O. K. Baranova, C. Coleman, H. E. Garcia, A. Grodsky, D. R. Johnson, R. A. Locarnini, A. V. Mishonov, T.D. O'Brien, C.R. Paver, J.R. Reagan, D. Seidov, I. V. Smolyar,

and M. M. Zweng, 2013: World Ocean Database 2013, NOAA Atlas NESDIS 72, S. Levitus, Ed., A. Mishonov, Technical Ed.; Silver Spring, MD, 209 pp., http://doi.org/10.7289/V5NZ85MT, 2013.

Brennan, S. T., Lowenstein, T. K., & Cendón, D. I. : The major-ion composition of Cenozoic seawater: The past 36 million years from fluid inclusions in marine halite. American Journal of Science, 313(8), 713-775, 2013.

Caves J. K., Jost A. B., Lau K. V. and Maher K.: Cenozoic carbon cycle imbalances and a variable weathering feedback. Earth Planet. Sci. Lett. 450, 152–163, 2016.

Chalk T. B., Hain M. P., Foster G. L., Rohling E. J., Sexton P. F., Badger M. P. S., Cherry S. G., Hasenfratz A. P., Haug G. H., Jaccard S. L., Martínez-García A., Pälike H., Pancost R. D. and Wilson P. A.: Causes of ice age intensification across the Mid-Pleistocene Transition. Proc. Natl. Acad. Sci., 201702143, 2017.

Coggon R. M., Teagle D. A. H. and Dunkley Jones T. Comment on "What do we know about the evolution of Mg to Ca ratios in seawater?" by Wally Broecker and Jimin Yu. Paleoceanography 26, 2011.

DeConto, R. M., & Pollard, D.: Rapid Cenozoic glaciation of Antarctica induced by declining atmospheric CO2. Nature, 421(6920), 245-249, 2003.

DeConto R. M., Pollard D., Wilson P. A., Pälike H., Lear C. H. and Pagani M.: Thresholds for Cenozoic bipolar glaciation. Nature 455, 652–656, 2008.

DeFantle M. S. and DePaolo D. J.: Sr isotopes and pore fluid chemistry in carbonate sediment of the Ontong Java Plateau: Calcite recrystallization rates and evidence for a rapid rise in seawater Mg over the last 10 million years. Geochim. Cosmochim. Acta 70, 3883–3904, 2006.

Dekens P. S., Lea D. W., Pak D. K. and Spero H. J.: Core top calibration of Mg/Ca in tropical foraminifera: Refining paleotemperature estimation. Geochemistry, Geophys. Geosystems 3, 1–29, 2002.

Delaney, M. L., Bé, A. W., & Boyle, E. A.: Li, Sr, Mg, and Na in foraminiferal calcite shells from laboratory culture, sediment traps, and sediment cores. Geochimica et Cosmochimica Acta, 49(6), 1327-1341, 1985.

de la Vega, E., Chalk, T. B., Wilson, P. A., Bysani, R. P., & Foster, G. L.: Atmospheric CO2 during the Mid-Piacenzian Warm Period and the M2 glaciation. Scientific Reports, 10(1), 1-8, 2020.

Dickson A. G.: Thermodynamics of the Dissociation of Boric Acid in Potassium Chloride Solutions from 273.15 to 318.15 K. J. Chem. Eng. Data 35, 253–257, 1990.

Drury, A. J., Lee, G. P., Gray, W. R., Lyle, M., Westerhold, T., Shevenell, A. E., & John, C. M.: Deciphering the state of the late Miocene to early Pliocene equatorial Pacific. Paleoceanography and paleoclimatology, 33(3), 246-263, 2018.

Dyez, K. A., Hönisch, B., & Schmidt, G. A.: Early Pleistocene obliquity-scale pCO2 variability at~ 1.5 million years ago. *Paleoceanography and Paleoclimatology*, *33*(11), 1270-1291, 2018.

Evans, D. & Müller, W.: Deep time foraminifera Mg/Ca paleothermometry: Nonlinear correction for secular change in seawater Mg/Ca. Paleoceanography 27, PA4205, 2012.

Evans, D., Wade, B. S., Henenhan, M., Erez, J., & Müller, W.: Revisiting carbonate chemistry controls on planktic foraminifera Mg/Ca: implications for sea surface temperature and hydrology shifts over the Paleocene–Eocene Thermal Maximum and Eocene–Oligocene transition. Climate of the Past, 12(4), 819-835, 2016.

Farmer, J. R., Hönisch, B., & Uchikawa, J.: Single laboratory comparison of MC-ICP-MS and N-TIMS boron isotope analyses in marine carbonates. Chemical Geology, 447, 173-182, 2016.

Farrell, J.W., Raffi, I., Janecek, T.,Murray, D.W., Levitan,M., Dadey, K.A., Emeis, K.C., Lyle, M., Flores, J.A., Hovan, S: Late Neogene sedimentation patterns in the eastern Equatorial Pacific Ocean. In: Pisias,N.G.,Mayer, L.A., Janecek, T.R., Palmer-Julson, A., van Andel, T.H. (Eds.), Proceedings of the Ocean Drilling Program. Scientific Results, vol. 138. ocean Drilling Program, College Station, TX, pp. 717–756, 1995.

Flower, B. P., & Kennett, J. P.: Middle Miocene deepwater paleoceanography in the southwest Pacific: relations with East Antarctic Ice Sheet development. Oceanographic Literature Review, 8(43), 796, 1996.

Flower, B. P., & Kennett, J. P.: Middle Miocene ocean-climate transition: High-resolution oxygen and carbon isotopic records from Deep Sea Drilling Project Site 588A, southwest Pacific. Paleoceanography, 8(6), 811-843, 1993.

Ford, H. L., Ravelo, A. C., Dekens, P. S., LaRiviere, J. P., & Wara, M. W.: The evolution of the equatorial thermocline and the early Pliocene El Padre mean state. Geophysical Research Letters, 42(12), 4878-4887, 2015.

Foster G. L.: Seawater pH, pCO2and [CO2-3] variations in the Caribbean Sea over the last 130 kyr: A boron isotope and B/Ca study of planktic foraminifera. Earth Planet. Sci. Lett. 271, 254–266, 2008.

Foster G. L. and Rohling E. J.: Relationship between sea level and climate forcing by CO2 on geological timescales. Proc. Natl. Acad. Sci. 110, 1209–1214, 2013.

Foster G. L. and Sexton P. F.: Enhanced carbon dioxide outgassing from the eastern equatorial Atlantic during the last glacial. Geology 42, 1003–1006, 2014.

Foster, G. L., Hönisch, B., Paris, G., Dwyer, G. S., Rae, J. W., Elliott, T., Gaillardet, J., Hemming, N. G., Louvat, P., Vengosh, A.: Interlaboratory comparison of boron isotope analyses of boric acid, seawater and marine CaCO3 by MC-ICPMS and NTIMS. Chemical Geology, 358, 1-14, 2013.

Foster G. L., Lear C. H. and Rae J. W. B.: The evolution of pCO2, ice volume and climate during the middle Miocene. Earth Planet. Sci. Lett. 341–344, 243–254, 2012.

Foster G. L., Royer D. L. and Lunt D. J.: Future climate forcing potentially without precedent in the last 420 million years. Nat. Commun. 8, 14845. http://dx.doi.org/10.1038/ncomms14845, 2017.

Gasson E., DeConto R. M., Pollard D. and Levy R. H.: Dynamic Antarctic ice sheet during the early to mid-Miocene. Proc. Natl. Acad. Sci. 113, 3459–3464, 2016.

Gothmann A. M., Stolarski J., Adkins J. F., Schoene B., Dennis K. J., Schrag D. P., Mazur M. and Bender M. L.: Fossil corals as an archive of secular variations in seawater chemistry since the Mesozoic. Geochim. Cosmochim. Acta 160, 188–208, 2015.

GraphPad Prism version 7.00 for Windows, GraphPad Software, La Jolla California USA, www.graphpad.com"

Gray, W. R., & Evans, D.: Nonthermal influences on Mg/Ca in planktonic foraminifera: a review of culture studies and application to the Last Glacial Maximum. Paleoceanography and Paleoclimatology, 34(3), 306-315, 2019.

Gray, W. R., Weldeab, S., Lea, D. W., Rosenthal, Y., Gruber, N., Donner, B., & Fischer, G.: The effects of temperature, salinity, and the carbonate system on Mg/Ca in Globigerinoides ruber (white): A global sediment trap calibration. Earth and Planetary Science Letters, 482, 607-620, 2018.

Greenop R., Foster G. L., Wilson P. A. and Lear C. H.: Middle Miocene climate instability associated with high-amplitude CO2 variability. Paleoceanography 29, 845–853, 2014.

Greenop R., Hain M. P., Sosdian S. M., Oliver K. I. C., Goodwin P., Chalk T. B., Lear C. H., Wilson P. A. and Foster G. L.: A record of Neogene seawater δ11B reconstructed from paired δ11B analyses on benthic and planktic foraminifera. Clim. Past 13, 149–170, 2017.

Guillermic, M., Misra, S., Eagle, R., Villa, A., Chang, F., Tripati, A.,: Seawater pH reconstruction using boron isotopes in multiple planktonic foraminifera species with different depth habitats and their potential to constrain pH and pCO2 gradients. Biogeosciences, 17(13), 3487-3510, 2020.

Gutjahr, M., Bordier, L., Douville, E., Farmer, J., Foster, G. L., Hathorne, E. C., J., Foster, G. L., Hathorne, E., Hönish, B., Lemarchand, D., Louvat, P., McCulloch, M., Noireaux, J., Pallavicini, N., Rodushkin, I., Roux, P., Stewart, J., Thil, F. You, C.F.Sub-permil interlaboratory consistency for solution-based boron isotope analyses on marine carbonates. *Geostandards and Geoanalytical Research*, 2020.

Hain, M. P., Foster, G. L., & Chalk, T.: Robust constraints on past CO2 climate forcing from the boron isotope proxy. Paleoceanography and Paleoclimatology, 33(10), 1099-1115, 2018.

Hansen, J., Sato, M., & Ruedy, R.: Perception of climate change. Proceedings of the National Academy of Sciences, 109(37), 2012.

Hansen J., Sato M., Russell G. and Kharecha P.: Climate sensitivity, sea level and atmospheric carbon dioxide. Philos. Trans. R. Soc. A Math. Phys. Eng. Sci. 371, 1–38, 2013.
Haug, G. H., & Tiedemann, R.: Effect of the formation of the Isthmus of Panama on Atlantic Ocean thermohaline circulation. Nature, 393(6686), 673-676, 1998.
Haywood, A. M., Dowsett, H. J., & Dolan, A. M.: Integrating geological archives and climate models for the mid-Pliocene warm period. Nature communications, 7(1), 1-14, 2016.
Hemming N. G. and Hanson G. N.: Boron isotopic composition and concentration in modern marine carbonates. Geochim. Cosmochim. Acta 56, 537–543, 1992.
Henehan M. J., Foster G. L., Bostock H. C., Greenop R., Marshall B. J. and Wilson P. A.: A new boron isotope-pH calibration for Orbulina universa, with implications for understanding and accounting for 'vital effects.' Earth Planet. Sci. Lett. 454, 282–292, 2016.
Henehan M. J., Rae J. W. B., Foster G. L., Erez J., Prentice K. C., Kucera M., Bostock H. C., Martínez-Botí M. A., Milton J. A., Wilson P. A., Marshall B. J. and Elliott T. (2013) Calibration of the boron isotope proxy in the planktonic foraminifera Globigerinoides ruber for use in palaeo-CO2reconstruction. Earth Planet. Sci. Lett. 364, 111–122, 2013.
Higgins J. A., Kurbatov A. V, Spaulding N. E., Brook E., Introne D. S., Chimiak L. M., Yan Y., Mayewski P. A. and Bender M. L.: Atmospheric composition 1 million years ago from blue ice in the Allan Hills, Antarctica. Proc. Natl. Acad. Sci. 112, 6887–6891, 2015.
Holbourn A., Kuhnt W., Frank M. and Haley B. A.: Changes in Pacific Ocean circulation following the Miocene onset of permanent Antarctic ice cover. Earth Planet. Sci. Lett. 365, 38–50, 2013.
Holcomb M., DeCarlo T. M., Schoepf V., Dissard D., Tanaka K. and McCulloch M.: Cleaning and pre-treatment procedures for biogenic and synthetic calcium carbonate powders for determination of elemental and boron isotopic compositions. Chem. Geol. 398, 11–21, 2015.
Hönisch, B. and Hemming, N. G., Ground-truthing the boron isotope-paleo-pH proxy in planktonic foraminifera shells: Partial dissolution and shell size effects, Paleoceanography 19, 1–13, 2004.
Honisch, B., Allen, K. A., Lea, D. W., Spero, H. J., Eggins, S. M., Arbuszewski, J., deMenocal, P., Rosenthal, Y., D. Russel, a.: Elderfield, H.: The influence of salinity on Mg/Ca in planktic foraminifers–Evidence from cultures, core-top sediments and complementary d 18 O. Geochimica Et Cosmochimica Acta, 121, 196-213, 2013.
Hönisch, B., Eggins, S. M., Haynes, L. L., Allen, K. A., Holland, K. D., & Lorbacher, K.: Boron Proxies in Paleoceanography and Paleoclimatology. John Wiley & Sons, 2019.
Hönisch B., Hemming N. G., Archer D., Siddall M. and McManus J. F.: Atmospheric carbon dioxide concentration across the mid-pleistocene transition. Science 324, 1551–1554, 2009.
Horita J., Zimmermann H. and Holland H. D.: Chemical evolution of seawater during the Phanerozoic: Implications from the record of marine evaporites. Geochim. Cosmochim. Acta 66, 3733–3756., 2002.
IPCC: Climate Change 2014 - The Physical Science Basis, edited by Intergovernmental Panel on Climate Change, Cambridge University Press, Cambridge., 2014.
IPCC: Global Warming of 1.5 ºC- edited by Intergovernmental Panel on Climate Change, 2018.
Johnstone, H. J., Lee, W., & Schulz, M.: Effect of preservation state of planktonic foraminifera tests on the decrease in Mg/Ca due to reductive cleaning and on sample loss during cleaning. Chemical Geology, 420, 23-36, 2016.
Kasbohm, J., & Schoene, B.: Rapid eruption of the Columbia River flood basalt and correlation with the mid-Miocene climate optimum. Science advances, 4(9), eaat8223, 2018.
Kennett, J. P., & Thunell, R. C.: On explosive Cenozoic volcanism and climatic implications. Science, 196(4295), 1231-1234, 1977.
Kısakürek, B., Eisenhauer, A., Böhm, F., Garbe-Schönberg, D., & Erez, J.: Controls on shell Mg/Ca and Sr/Ca in cultured planktonic foraminiferan, Globigerinoides ruber (white). Earth and Planetary Science Letters, 273(3-4), 260-269, 2008.
Klochko K., Kaufman A. J., Yao W., Byrne R. H. and Tossell J. A.: Experimental measurement of boron isotope fractionation in seawater. Earth Planet. Sci. Lett. 248, 261–270, 2006.
Koenig S. J., DeConto R. M. and Pollard D.: Late Pliocene to Pleistocene sensitivity of the Greenland Ice Sheet in response to external forcing and internal feedbacks. Clim. Dyn. 37, 1247–1268, 2011.

Kroenke, L. W., Berger, W. H., Janecek, T. R. and Shipboard Scientific Party: Proceedings of the Ocean Drilling Program, Initial Reports, Vol. 130, 1991.
Lea, D. W.: The 100 000-yr cycle in tropical SST, greenhouse forcing, and climate sensitivity. Journal of Climate, 17(11), 2170-2179, 2004.
Lee, K., Kim, T. W., Byrne, R. H., Millero, F. J., Feely, R. A., & Liu, Y. M.: The universal ratio of boron to chlorinity for the North Pacific and North Atlantic oceans. Geochimica et Cosmochimica Acta, 74(6), 1801-1811, 2010.
Lea, D. W., Pak, D. K., & Spero, H. J.: Climate impact of late Quaternary equatorial Pacific sea surface temperature variations. Science, 289(5485), 1719-1724, 2000.
Lear, C. H., Coxall, H. K., Foster, G. L., Lunt, D. J., Mawbey, E. M., Rosenthal, .Y., Sosdian, S. M., Thomas, E.,& Wilson, P. A.: Neogene ice volume and ocean temperatures: Insights from infaunal foraminiferal Mg/Ca paleothermometry. Paleoceanography, 30(11), 1437-1454, 2015.
Lemarchand D., Gaillardet J., Lewin and Allégre C. J.: The influence of rivers on marine boron isotopes and implications for reconstructing past ocean pH. Nature 408, 951–954, 2000.
Lisiecki L. E. and Raymo M. E.: A Pliocene-Pleistocene stack of 57 globally distributed benthic δ18O records. Paleoceanography 20, 1–17, 2005.
Lloyd, N. S., Sadekov, A. Y. and Misra, S., Application of 1013ohm Faraday cup current amplifiers for boron isotopic analyses by solution mode and laser ablation multicollector inductively coupled plasma mass spectrometry, Rapid Commun. Mass Spectrom., 32, 9–18, 2018.
Lueker, T. J., Dickson, A. G., & Keeling, C. D.: Ocean pCO2 calculated from dissolved inorganic carbon, alkalinity, and equations for K1 and K2: validation based on laboratory measurements of CO2 in gas and seawater at equilibrium. Marine chemistry, 70(1-3), 105-119, 2000.
Lunt D. J., Foster G. L., Haywood A. M. and Stone E. J.: Late Pliocene Greenland glaciation controlled by a decline in atmospheric CO_2 levels. Nature 454, 1102–1105, 2008.
Lunt, D. J., Haywood, A. M., Schmidt, G. A., Salzmann, U., Valdes, P. J., & Dowsett, H. J.: Earth system sensitivity inferred from Pliocene modelling and data. Nature Geoscience, 3(1), 60-64, 2010.
Lüthi D., Le Floch M., Bereiter B., Blunier T., Barnola J. M., Siegenthaler U., Raynaud D., Jouzel J., Fischer H., Kawamura K. and Stocker T. F.: High-resolution carbon dioxide concentration record 650,000-800,000 years before present. Nature 453, 379–382, 2008.
Martínez-Botí, M. A., Marino G., Foster G. L., Ziveri P., Henehan M. J., Rae J. W. B., Mortyn P. G. and Vance D.: Boron isotope evidence for oceanic carbon dioxide leakage during the last deglaciation. Nature 518, 219–222, 2015b.
Martínez-Garcia, A., Rosell-Melé, A., Jaccard, S. L., Geibert, W., Sigman, D. M., & Haug, G. H.: Southern Ocean dust–climate coupling over the past four million years. *Nature*, *476*(7360), 312-315, 2011.
Mavromatis, V., Montouillout, V., Noireaux, J., Gaillardet, J. and Schott, J., Characterization of boron incorporation and speciation in calcite and aragonite from co-precipitation experiments under controlled pH, temperature and precipitation rate, Geochim. Cosmochim. Acta, 150, 299–313, 2015.
McCulloch M. T., Holcomb M., Rankenburg K. and Trotter J. A.: Rapid, high-precision measurements of boron isotopic compositions in marine carbonates. Rapid Commun. Mass Spectrom. 28, 2704–2712, 2014.
Medina-Elizalde M. and Lea D. W.: The mid-pleistocene transition in the tropical pacific. Science 310, 1009–1012, 2005.
Misra, S. and Froelich, P. N.: Lithium isotope history of cenozoic seawater: Changes in silicate weathering and reverse weathering. Science (80-.). 335, 818–823, 2012.
Misra, S., Greaves, M., Owen, R., Kerr, J., Elmore, A. C. and Elderfield, H.: Determination of B/Ca of natural carbonates by HR-ICP-MS. Geochemistry, Geophys. Geosystems 15, 1617–1628, 2014a.
Misra, S., Owen, R., Kerr, J., Greaves, M. and Elderfield, H.: Determination of δ11B by HR-ICP-MS from mass limited samples: Application to natural carbonates and water samples. Geochim. Cosmochim. Acta 140, 531–552, 2014b.

Nathan, S. A., & Leckie, R. M.: Palaeogeography, Palaeoclimatology, Palaeoecology, 274(3-4), 140-159, 2009.
Ni Y., Foster G. L., Bailey T., Elliott T., Schmidt D. N., Pearson P., Haley B. and Coath C.: A core top assessment of proxies for the ocean carbonate system in surface-dwelling foraminifers. Paleoceanography 22, 2007.
Nir O., Vengosh A., Harkness J. S., Dwyer G. S. and Lahav O.: Direct measurement of the boron isotope fractionation factor: Reducing the uncertainty in reconstructing ocean paleo-pH. Earth Planet. Sci. Lett. 414, 1–5, 2015.
Nürnberg, D., Bijma, J., & Hemleben, C.: Assessing the reliability of magnesium in foraminiferal calcite as a proxy for water mass temperatures. Geochimica et Cosmochimica Acta, 60(5), 803-814, 1996.
O'Brien C. L., Foster G. L., Martínez-Botí M. A., Abell R., Rae J. W. B. and Pancost R. D.: High sea surface temperatures in tropical warm pools during the Pliocene. Nat. Geosci. 7, 606–611, 2014.
Osborne, E. B., Umling, N. E., Bizimis, M., Buckley, W., Sadekov, A., Tappa, E., Marshall, B., R. Sautter, L., Thunell, R. C.: A Sediment Trap Evaluation of B/Ca as a Carbonate System Proxy in Asymbiotic and Nondinoflagellate Hosting Planktonic Foraminifera. Paleoceanography and Paleoclimatology, 35(2), 2020.
Pagani P., Freeman G., Arthur F., Schuster M., Tiercelin J.-J. and Brunet M.: Late miocene atmospheric CO(2) concentrations and the expansion of C(4) grasses. Science 285, 876–9, 1999.
Pagani M., Liu Z., Lariviere J. and Ravelo A. C.: High Earth-system climate sensitivity determined from Pliocene carbon dioxide concentrations. Nat. Geosci. 3, 27–30, 2010.
Pagani M., Zachos J. C., Freeman K. H., Tipple B. and Bohaty S.: Atmospheric science: Marked decline in atmospheric carbon dioxide concentrations during the Paleogene. Science 309, 600–603, 2005.
Pearson, P. N., & Palmer, M. R.: Atmospheric carbon dioxide concentrations over the past 60 million years. *Nature*, *406*(6797), 695-699, 2000.
Perez, F. F., & Fraga, F.: Association constant of fluoride and hydrogen ions in seawater. Marine Chemistry, 21(2), 161-168, 1987.
Petit J. R., Jouzel J., Raynaud D., Barkov N. I., Barnola J. M., Basile I., Bender M., Chappellaz J., Davis M., Delaygue G., Delmotte M., Kotiyakov V. M., Legrand M., Lipenkov V. Y., Lorius C., Pépin L., Ritz C., Saltzman E. and Stievenard M.: Climate and atmospheric history of the past 420,000 years from the Vostok ice core, Antarctica. Nature 399, 429–436, 1999.
Pierrot, D., Lewis, E., & Wallace, D. W. R.: MS Excel program developed for CO2 system calculations. ORNL/CDIAC-105a. Carbon Dioxide Information Analysis Center, Oak Ridge National Laboratory, US Department of Energy, Oak Ridge, Tennessee, 10, 2006.
Premoli Silva, L, Haggerty, J., Rack, F., et al.: Proceedings of the Ocean Drilling Program, Initial Reports, Vol. 144, 1993.
Rae, J. W., Zhang, Y. G., Liu, X., Foster, G. L., Stoll, H. M., & Whiteford, R. D.: Atmospheric CO_2 over the Past 66 Million Years from Marine Archives. Annual Review of Earth and Planetary Sciences, 49, 2021.
Raitzsch M. and Hönisch B.: Cenozoic boron isotope variations in benthic foraminifers. Geology 41, 591–594, 2013.
Raitzsch M., Bijma J., Benthien A., Richter K. U., Steinhoefel G. and Kučera M.: Boron isotope-based seasonal paleo-pH reconstruction for the Southeast Atlantic – A multispecies approach using habitat preference of planktonic foraminifera. Earth Planet. Sci. Lett. 487, 138–150, 2018.
Raitzsch, M., Bijma, J., Bickert, T., Schulz, M., Holbourn, A., & Kučera, M.: Atmospheric carbon dioxide variations across the middle Miocene climate transition. Climate of the Past, 17(2), 703-719, 2021.
Ravelo, A. C., Lawrence, K. T., Fedorov, A., & Ford, H. L.: Comment on "A 12-million-year temperature history of the tropical Pacific Ocean". Science, 346(6216), 1467-1467, 2014.
Retallack G. J.: Greenhouse crises of the past 300 million years. Geol. Soc. Am. Bull. 121, 1441–1455, 2009.
Rickaby, R. E. M. and Halloran, P.: Cool La Nina During the Warmth of the Pliocene?, Science, 307, 1948–1952, 2005.

Ridgwell A. and Zeebe R. E.: The role of the global carbonate cycle in the regulation and evolution of the Earth system. Earth Planet. Sci. Lett. 234, 299–315, 2005.
Royer D. L.: Stomatal density and stomatal index as indicators of paleoatmospheric CO2 concentration. Rev. Palaeobot. Palynol. 114, 1–28, 2001.
Rowley, D. B.: Rate of plate creation and destruction: 180 Ma to present. Geological Society of America Bulletin, 114(8), 927-933, 2002.
Russell, A. D., Hönisch, B., Spero, H. J., & Lea, D. W.: Effects of seawater carbonate ion concentration and temperature on shell U, Mg, and Sr in cultured planktonic foraminifera. Geochimica et Cosmochimica Acta, 68(21), 4347-4361, 2004.
Schmittner, A., Urban, N. M., Shakun, J. D., Mahowald, N. M., Clark, P. U., Bartlein, P. J., Mix A. C., Rosell-Melé, A.: Climate sensitivity estimated from temperature reconstructions of the Last Glacial Maximum. Science, 334(6061), 1385-1388, 2011.
Seki O., Foster G. L., Schmidt D. N., Mackensen A., Kawamura K. and Pancost R. D.: Alkenone and boron-based Pliocene pCO2records. Earth Planet. Sci. Lett. 292, 201–211, 2010.
Shackleton N.J. , Berger A., Peltier W.R,: Trans. R. Soc. Edinb. Earth Sci. 81, 251. Shipboard Leg, O. D. P., Map, O. D. P., & Map, D. S. D.: P. Initial Reports: Volume 130. doi:10.2973/odp.proc.ir.130.108.1991, 1991.
Shuttleworth, R., Bostock, H. C., Chalk, T. B., Calvo, E., Jaccard, S. L., Pelejero, C., Martínez-Garcia, A., & Foster, G. L. (2021). Early deglacial CO2 release from the Sub-Antarctic Atlantic and Pacific oceans. Earth and planetary science letters, 554, 116649.
Shevenell, A. E., Kennett, J. P., & Lea, D. W.: Middle Miocene southern ocean cooling and Antarctic cryosphere expansion. *Science*, *305*(5691), 1766-1770, 2004.
Schlitzer, R., Ocean Data View, https://odv.awi.de, 2016.
Siegenthaler, U., Stocker, T. F., Monnin, E., Lüthi, D., Schwander, J., Stauffer, B, Raynaud, D., Barnola, JM., Fischer, H., Masson-Delmotte, V., Jouzel, J.: Stable carbon cycle–climate relationship during the late Pleistocene. Science, 310(5752), 1313-1317, 2005.
Sosdian, S. M., Babila, T. L., Greenop, R., Foster, G. L., & Lear, C. H.: Ocean carbon storage across the middle Miocene: A new interpretation for the Monterey Event. Nature communications, 11(1), 1-11, 2020.
Sosdian, S. M., Greenop R., Hain M. P., Foster G. L., Pearson P. N. and Lear C. H.: Constraining the evolution of Neogene ocean carbonate chemistry using the boron isotope pH proxy. Earth Planet. Sci. Lett. 498, 362–376, 2018.
Stap L. B., de Boer B., Ziegler M., Bintanja R., Lourens L. J. and van de Wal R. S. W.: CO_2 over the past 5 million years: Continuous simulation and new δ11B-based proxy data. Earth Planet. Sci. Lett. 439, 1–10, 2016.
Stoll, H. M., Guitian, J., Hernandez-Almeida, I., Mejia, L. M., Phelps, S., Polissar, P., Rosenthal, Y., Zhang, H. & Ziveri, P.: Upregulation of phytoplankton carbon concentrating mechanisms during low CO2 glacial periods and implications for the phytoplankton pCO2 proxy. Quaternary Science Reviews, 208, 1-20, 2019.
Super, J. R., Thomas, E., Pagani, M., Huber, M., O'Brien, C., & Hull, P. M.: North Atlantic temperature and pCO_2 coupling in the early-middle Miocene. *Geology*, *46*(6), 519-522, 2018.
Super, J. R., Thomas, E., Pagani, M., Huber, M., O'Brien, C. L., & Hull, P. M.: Miocene Evolution of North Atlantic Sea Surface Temperature. Paleoceanography and Paleoclimatology, 35(5), 2020.
Sutton J. N., Liu Y.-W., Ries J. B., Guillermic M., Ponzevera E. and Eagle R. A.: δ11B as monitor of calcification site pH in divergent marine calcifying organisms. Biogeosciences 15, 1447–1467, 2018.
Takahashi T., Sutherland S. C., Chipman D. W., Goddard J. G. and Ho C.: Climatological distributions of pH, pCO2, total CO2, alkalinity, and CaCO3saturation in the global surface ocean, and temporal changes at selected locations. Mar. Chem. 164, 95–125, 2014.
Tan, N., Ramstein, G., Dumas, C., Contoux, C., Ladant, J. B., Sepulchre, P., Zhang, Z., De Schepper, S.: Exploring the MIS M2 glaciation occurring during a warm and high atmospheric CO2 Pliocene background climate. Earth and Planetary Science Letters, 472, 266-276, 2017.

Tanner, T., Hernández-Almeida, I., Drury, A. J., Guitián, J., & Stoll, H.: Decreasing atmospheric CO_2 during the late Miocene Cooling. *Paleoceanography and Paleoclimatology*, e2020PA003925, 2020.
Tierney, J. E., Zhu, J., King, J., Malevich, S. B., Hakim, G. J., & Poulsen, C. J.: Glacial cooling and climate sensitivity revisited. *Nature*, *584*(7822), 569-573, 2020.
Thomas, E.: Descent into the Icehouse. Geology 36, 191–192, 2008.
Toggweiler, J. R.: Variation of atmospheric CO_2 by ventilation of the ocean's deepest water. Paleoceanography, 14(5), 571-588, 1999.
Tripati, A., & Darby, D.: Evidence for ephemeral middle Eocene to early Oligocene Greenland glacial ice and pan-Arctic sea ice. Nature communications, 9(1), 1-11, 2018
Tripati A. K., Roberts C. D. and Eagle R. A.: Coupling of CO2and Ice sheet stability over major climate transitions of the last 20 million years. Science (80). 326, 1394–1397, 2009.
Tripati A. K., Roberts C. D., Eagle R. A. and Li G.: A 20 million year record of planktic foraminiferal B/Ca ratios: Systematics and uncertainties in pCO2reconstructions. Geochim. Cosmochim. Acta 75, 2582–2610. http://dx.doi.org/10.1016/j.gca.2011.01.018, 2011.
Tyrrell, T., & Zeebe, R. E.: History of carbonate ion concentration over the last 100 million years. Geochimica et Cosmochimica Acta, 68(17), 3521-3530, 2004.
Van Der Burgh J., Visscher H., Dilcher D. L. and Kürschner W. M.: Paleoatmospheric signatures in Neogene fossil leaves. Science 260, 1788–1790, 1993.
Vogl J. and Rosner M.: Production and Certification of a Unique Set of Isotope and Delta Reference Materials for Boron Isotope Determination in Geochemical, Environmental and Industrial Materials. Geostand. Geoanalytical Res. 36, 161–175, 2012.
Wara M. W., Ravelo A. C. and Delaney M. L.: Climate change: Permanent El Niño-like conditions during the Pliocene warm period. Science 309, 758–761, 2005.
Yan, Y., Bender, M. L., Brook, E. J., Clifford, H. M., Kemeny, P. C., Kurbatov, A. V., Mackay, S., Mayewski, P.A., Ng, J., Severinghaus, J.P., Higgins, J. A.: Two-million-year-old snapshots of atmospheric gases from Antarctic ice. Nature, 574(7780), 663-666, 2019.
Yu, J., Elderfield, H., Greaves, M., & Day, J.: Preferential dissolution of benthic foraminiferal calcite during laboratory reductive cleaning. Geochemistry, Geophysics, Geosystems, 8(6), 2007a.
Yu J., Elderfield H. and Hönisch B.: B/Ca in planktonic foraminifera as a proxy for surface seawater pH. Paleoceanography 22, 2007.
Zachos J. C., Dickens G. R. and Zeebe R. E.: An early Cenozoic perspective on greenhouse warming and carbon-cycle dynamics. Nature 451, 279–283, 2008.
Zachos, J., Pagani, M., Sloan, L., Thomas, E., & Billups, K.: Trends, rhythms, and aberrations in global climate 65 Ma to present. science, 292(5517), 686-693, 2001.
Zeebe R. E. and Wolf-Gladrow D.: CO2 in Seawater: Equilibrium, Kinetics, Isotopes Elsevier Oceanography Series 65, Amsterdam, 2001.
Zhang Y. G., Pagani M., Liu Z., Bohaty S. M. and Deconto R.: A 40-million-year history of atmospheric CO2. Philos. Trans. R. Soc. A Math. Phys. Eng. Sci. 371, 20130096–20130096, 2013.
Zhang, Y. G., Pagani, M., & Liu, Z.: A 12-million-year temperature history of the tropical Pacific Ocean. *Science*, *344*(6179), 84-87, 2014.
Zhang, J., Wang, P., Li, Q., Cheng, X., Jin, H., & Zhang, S.: Western equatorial Pacific productivity and carbonate dissolution over the last 550 kyr: Foraminiferal and nannofossil evidence from ODP Hole 807A. Marine Micropaleontology, 64(3-4), 121-140, 2007.

Figure captions

Figure 1: Modern hydrography of sites. **A.** Map of air-sea pCO_2 (ΔpCO_2, ppm, data from Takahashi et al. (2014) and plotted using Ocean Data View from Schlitzer, (2016) showing the location of ODP Sites 806 and 807 (black circles) and Site 872 (black square, Premoli et al., 1993). Depth profiles are for preindustrial parameters, **B.** pH calculated from GLODAP database and corrected from anthropogenic inputs, **C.** Boron isotopic composition of borate ion ($\delta^{11}B_{borate}$) with associated propagated uncertainties.

Figure 2: Foraminiferal data for the Miocene to Recent. **A.** Benthic foraminiferal $\delta^{18}O$ data (blue line – stack from Lisiecki and Raymo, 2005; black line – compilation from Zachos et al., 2008). **B.** $\delta^{11}B$ of *T. sacculifer* (blue circles) and *G. rube*r (blue triangles) at Sites 806 (light blue), 807 (dark blue), Grey filled square are data from Site 872 located in the WEP (Sosdian et al., 2018). Open symbols are $\delta^{11}B$ data from published studies (Hönisch and Hemming, 2009; Seki et al., 2010; Foster et al., 2012; Greenop et al., 2014; Martinez-Boti et al., 2015a; Chalk et al., 2017; Dyez et al., 2018; Sosdian et al., 2018; de la Vega et al., 2020; Raitzsch et al., 2021), grey open symbols are *T. sacculifer*, brown open symbols are for *G. ruber.* **C.** Mg/Ca ratios of *T. sacculifer* and *G. rube*r at Sites 806, 807 and fourth-order polynomial regression from Sosdian et al. (2020) representing secular variations of Mg/Ca_{sw} (blue dotted line). **E.** Calculated weight per shell for *T. sacculifer* and *G. ruber*. For Panels B-D: Circles = *T. sacculifer,* Triangles = *G. ruber.*

Figure 3: A. Reconstruction of surface pCO_2 (ppm) for the past 0.8 Myr from *T. sacculifer* at ODP Sites 806 and 807 (blue symbols) using boron-based pH calculated from $\delta^{11}B_{seawater}$ (Greenop et al., 2017) and alkalinity from Caves et al. (2016). Planktonic foraminiferal $\delta^{18}O$ at site 806 with isotope stages labeled (black line – Medina-Elizalde and Lea, 2005) and benthic foraminiferal $\delta^{18}O$ stack (grey line - Lisiecki and Raymo, 2005), benthic $\delta^{18}O$ at Site 806 (dark red line) from Lear et al. (2003, 2015). **B.** pCO_2 values calculated from boron isotopes (colored symbols - this study) with data from the literature (open gray triangles – compilation B are data recalculated in Rae et al., 2021) and ice core pCO_2 (black line – Petit et al., 1999, Lüthi et al., 2008, Bereiter et al., 2015). **C.** Cross plot for the last 0.8 Myr of $pCO_{2T.\ sacculifer}$ from this study and pCO_2_ice core (from ice core compilation, Bereiter et al., 2015), grey line is a simple linear regression: p = 0.25, R^2=0.09, blue line is a Deming regression with bootstrap (n=1000) taking into account both x and y uncertainties (p = 0.25), ice core CO_2 error calculated based 2 SD on ± 1 ky on the age determined from age model and boron based pCO_2 error is calculated based on error propagation eq. S17, outputs of the regression are presented in Table S6. Data compiled are from: Foster et al., 2008; Hönisch and Hemming, 2009; Seki et al., 2010; Foster et al., 2012; Badger et al., 2013; Greenop et al., 2014; Martinez-Boti et al., 2015a; Chalk et al., 2017; Dyez et al., 2018; Sosdian et al., 2018; Greenop et al., 2019; de la Vega et al., 2020.

Figure 4: Compilation of temperature from site 806 in the WEP. Mg/Ca based temperature were derived using the same framework (see supplemental information). Blue filled symbols are from Sites 806 and 807 with blue circles for *T. sacculifer* and triangles for *G. ruber*; filled gray squares are data from Site 872 (Sosdian et al., 2018). Open symbols are SST derived from Mg/Ca at Site 806 (Wara et al., 2005; Tripati et al., 2009; Nathan and Leckie, 2009). Tex_{86} and $U^{K'}_{37}$ are also plotted for comparison (Zhang et al., 2014). Orange open circles are SST data calculated with our framework from the species *D. altispera* at ODP Site 806 (Sosdian et al., 2020) with an offset of +8°C. Blue line is a smooth line (Lowess) going through the data.

Figure 5: Different models for the evolution of the boron geochemistry explored as part of this work. Due to the 1 ‰ uncertainty propagated for $\delta^{11}B_{seawater}$, all scenarios yield reconstructed seawater pH values that are within error of each other. Propagated uncertainties were calculated using eq. S14 (see Supplement). **A.** Different models for $\delta^{11}B_{seawater}$ used for the reconstruction of pCO_2 in this study (blue – Lemarchand et al., 2000; green – Greenop et al., 2017; red – Raitzsch and Hönisch, 2013). **B**. Reconstructed pH based on our measured $\delta^{11}B_{carbonate}$ values using different models for $\delta^{11}B_{seawater}$ (blue – Lemarchand et al., 2000; green – Greenop et al., 2017; red – Raitzsch and Hönisch, 2013),

compilations of pH from Sosdian et al. (2018) (compilation A - open squares) and Rae et al. (2021) (compilation B - open triangles) are also shown for comparison. Data for compilation A are from: Hönisch and Hemming, 2009; Seki et al., 2010; Foster et al., 2012; Badger et al., 2013; Greenop et al., 2014; Martinez-Boti et al., 2015a; Chalk et al., 2017; Sosdian et al., 2018. Data for compilation B are from: Foster et al., 2008; Hönisch and Hemming, 2009; Seki et al., 2010; Foster et al., 2012; Badger et al., 2013; Greenop et al., 2014; Martinez-Boti et al., 2015a; Chalk et al., 2017; Dyez et al., 2018; Sosdian et al., 2018; Greenop et al., 2019; de la Vega et al., 2020.

Figure 6: Different models for the evolution of a second carbonate (e.g. alkalinity) system parameter explored as part of this work. The propagated uncertainties were calculated using eq. S16 (see Supplement). **A**. Different models for alkalinity used for the reconstruction of pCO_2 in this study (brown – constant alkalinity of 2330 µmol/kg, blue - Ridgwell and Zeebe, 2005; green - Tyrell and Zeebe, 2004; violet - Caves et al., 2016. Colored symbols are reconstructed pCO_2 based on our measured $\delta^{11}B_{carbonate}$ values , alkalinity scenario and $\delta^{11}B_{seawater}$ from Greenop et al., 2017; open squares (compilation A) are pCO_2 compilation from Sosdian et al. (2018), open triangles (compilation B) are from compilation from Rae et al. (2021), black symbols are from site 872. **B.** Reconstructed pCO_2 using constant alkalinity of 2330 µmol/kg and $\delta^{11}B_{seawater}$ from Greenop et al. (2017). **C.** Reconstructed pCO_2 using constant alkalinity scenario from Ridgwell and Zeebe, (2005) and $\delta^{11}B_{seawater}$ from Greenop et al. (2017). **D.** Reconstructed pCO_2 using constant alkalinity scenario from Tyrell and Zeebe, (2004) and $\delta^{11}B_{seawater}$ from Greenop et al. (2017). **E.** Reconstructed pCO_2 using constant alkalinity scenario from Caves et al., (2016) and $\delta^{11}B_{seawater}$ from Greenop et al. (2017). In black are published estimates from ice core data (circles - Yan et al., 2019). Compilations of pCO_2 from Sosdian et al. (2018) (compilation A - open squares) and Rae et al. (2021) (compilation B - open triangles) are also shown for comparison. Data for compilation A are from: Hönisch and Hemming, 2009; Seki et al., 2010; Foster et al., 2012; Badger et al., 2013; Greenop et al., 2014; Martinez-Boti et al., 2015a; Chalk et al., 2017; Sosdian et al., 2018. Data for compilation B are from: Foster et al., 2008; Hönisch and Hemming, 2009; Seki et al., 2010; Foster et al., 2012; Badger et al., 2013; Greenop et al., 2014; Martinez-Boti et al., 2015a; Chalk et al., 2017; Dyez et al., 2018; Sosdian et al., 2018; Greenop et al., 2019; de la Vega et al., 2020. Stars indicate pCO_2 values reconstructed from alkenones by Tanner et al. (2020) (simulation 6) at Site 1088 in the Southern Ocean.

Figure 7: Proxy data for the past 22 million years in the Western Equatorial Pacific compared to benthic oxygen isotope data. **A.** Benthic $\delta^{18}O$ (blue line – stack from Lisiecki and Raymo, 2005; black line – compilation from Zachos et al., 2008). **B.** Benthic $\delta^{13}C$ (black line – compilation from Zachos et al., 2008). **C to E**, colored is indicating the site (filled light blue=806, filled dark blue=807), symbols represent the species (circle=*T. sacculifer* and triangle=*G. ruber*), filled grey squares are recalculated data based on Sosdian et al. (2018) at site 872. **C.** SST reconstructed at ODP Sites 806 and 807 using Mg/Ca ratios (see supplemental informations for reconstruction details), open symbols are reconstructed temperature based on literature Mg/Ca at site 806 (see text or Fig. 4). **D.** Seawater pH reconstructed from $\delta^{11}B$ of *T. sacculifer* and *G. ruber* using $\delta^{11}B_{seawater}$ from Greenop et al. (2017) (refer to text and supplement for calculations, this study), open squares (compilation A) are compilation data from Sosdian et al. (2018) and open triangles (compilation B) are compilation from Rae et al. (2021). **E.** Reconstructed pCO_2 (ppm) using boron-based pH and alkalinity from Caves et al. (2016), data presented are from this study. Propagated uncertainties are given by eq. S17 for the dark blue envelope, while the light blue envelope are the uncertainties calculated based on eq. S16 (taking into account uncertainty on $\delta^{11}B_{seawater}$). Crosses are original pCO_2 calculated in Sosdian et al. (2018) at Site 872; asterisks are recalculated pCO_2 at Site 872 by Rae et al. (2021).

Figure 8: Proxy data from 22 to 6 million years, including the Middle Miocene Climate Transition (MMCT) and Miocene Climate Optimum (MCO), in the Western Equatorial Pacific compared to benthic oxygen isotope data. **A.** Benthic $\delta^{18}O$ (black line – compilation from Zachos et al., 2008). **B.** Benthic $\delta^{13}C$ (black line – compilation from Zachos et al., 2008). **C and D**, colored is indicating the site (filled light blue=806, filled dark blue=807), symbols represent the species (circle=*T. sacculifer*

and triangle=*G. ruber*), filled grey squares are recalculated data based on Sosdian et al. (2018) at site 872. **C**. SST reconstructed at ODP Sites 806 and 807 using Mg/Ca ratios (see supplemental informations for reconstruction details), open symbols are reconstructed temperature based on litearature Mg/Ca at site 806 (see text or Fig. 4). **D.** Reconstructed pCO_2 (ppm) from this study (blue symbols) using boron-based pH and alkalinity from Caves et al. (2016). Propagated uncertainties are given by eq. S17 for the dark blue envelope, while the light blue envelope reflects the uncertainties calculated based on eq. S16 (taking into account uncertainty on $\delta^{11}B_{seawater}$). Orange datapoints and envelope are calculated pCO_2 and associated uncertainty from our study using our framework and a constant alkalinity scenario. Open squares (compilation A) are compilation data from Sosdian et al. (2018), open triangles are data from Raitzsch et al. (2021) at Site 1092. Crosses are original pCO_2 calculated in Sosdian et al. (2018) at Site 872; asterisks are recalculated pCO_2 at Site 872 by Rae et al. (2021); dark red triangles are from Site 1092 (Raitzsch et al., 2021). Data for compilation A are from: Hönisch and Hemming, 2009; Seki et al., 2010; Foster et al., 2012; Badger et al., 2013; Greenop et al., 2014; Martinez-Boti et al., 2015a; Chalk et al., 2017; Sosdian et al., 2018. Data for compilation B are from: Foster et al., 2008; Hönisch and Hemming, 2009; Seki et al., 2010; Foster et al., 2012; Badger et al., 2013; Greenop et al., 2014; Martinez-Boti et al., 2015a; Chalk et al., 2017; Dyez et al., 2018; Sosdian et al., 2018; Greenop et al., 2019; de la Vega et al., 2020.

Figure 9: Proxy data from 7 to 1 million years, including the Warm Pliocene Transition (WPT), in the Western Equatorial Pacific compared to benthic oxygen isotope data. **A.** Benthic $\delta^{18}O$ (black line – compilation from Zachos et al., 2008). **B.** Benthic $\delta^{13}C$ (black line – compilation from Zachos et al., 2008). **C and D**, colored is indicating the site (filled light blue=806, filled dark blue=807), symbols represent the species (circle=*T. sacculifer* and triangle=*G. ruber*), filled grey squares are recalculated data based on Sosdian et al. (2018) at ODP Site 872. **C**. SST reconstructed at ODP Sites 806 and 807 using Mg/Ca ratios (see supplemental informations for reconstruction details), open symbols are reconstructed temperature based on litearature Mg/Ca at site 806 (see text or Fig. 4). **D.** Reconstructed pCO_2 (ppm) from this study (blue symbols) using boron-based pH and alkalinity from Caves et al. (2016). Propagated uncertainties are given by eq. S17 for the dark blue envelope, while the light blue envelope reflects the uncertainties calculated based on eq. S16 (taking into account uncertainty on $\delta^{11}B_{seawater}$). Open squares (compilation A) are pCO_2 compilation from Sosdian et al. (2018), open triangles (compilation B) are from compilation from Rae et al. (2021). Data for compilation A are from: Hönisch and Hemming, 2009; Seki et al., 2010; Foster et al., 2012; Badger et al., 2013; Greenop et al., 2014; Martinez-Boti et al., 2015a; Chalk et al., 2017; Sosdian et al., 2018. Data for compilation B are from: Foster et al., 2008; Hönisch and Hemming, 2009; Seki et al., 2010; Foster et al., 2012; Badger et al., 2013; Greenop et al., 2014; Martinez-Boti et al., 2015a; Chalk et al., 2017; Dyez et al., 2018; Sosdian et al., 2018; Greenop et al., 2019; de la Vega et al., 2020. In black are published estimates from ice core data (circles - Yan et al., 2019).

Figure 10: Proxy data from 1.5 to 0.5 million years, including the Middle Pleistocene Transition (MPT), in the Western Equatorial Pacific compared to benthic oxygen isotope data. **A.** Benthic $\delta^{18}O$ (blue line – stack from Lisiecki and Raymo, 2005). **B.** Benthic $\delta^{13}C$ (black line – compilation from Zachos et al., 2008). **C and D** colored is indicating the site (filled light blue=806, filled dark blue=807), symbols represent the species (circle=*T. sacculifer* and triangle=*G. ruber*), filled grey squares (compilation A) are recalculated data based on Sosdian et al. (2018) at site 872. **C**. SST reconstructed at ODP Sites 806 and 807 using Mg/Ca ratios (see supplemental informations for reconstruction details), open symbols are reconstructed temperature based on litearature Mg/Ca at site 806 (see text or Fig. 4). **D.** Reconstructed pCO_2 (ppm) from this study (blue symbols) using boron-based pH and alkalinity from Caves et al. (2016). Propagated uncertainties are given by eq. S17. In black are published estimates from ice core data (line – Bereiter et al., 2015; black circles - Yan et al., 2019). Open triangles (compilation B) are from compilation from Rae et al. (2021). Data for compilation B are from: Foster et al., 2008; Hönisch and Hemming, 2009; Seki et al., 2010; Foster et al., 2012; Badger et al., 2013; Greenop et al., 2014; Martinez-Boti et al., 2015a; Chalk et al., 2017; Dyez et al., 2018; Sosdian et al., 2018; Greenop et al., 2019; de la Vega et al., 2020.

Figure 11: Proxy data from 1.5 to 0.5 million years, including the Middle Pleistocene Transition (MPT), in the Western Equatorial Pacific compared to benthic oxygen isotope composites. **A.** Benthic $\delta^{18}O$ (blue line – compilation from Lisiecki and Raymo, 2005, black line – compilation from Zachos et al. 2008). **B.** Records from Lithium isotopes ($\delta^{7}Li$, orange, Misra and Froelich, 2012) and Strontium isotopes ($^{87/86}Sr$, grey, Hodell et al., 1991, Farrel et al., 1995, Martin et al., 1999, Martin et al., 2004), both proxies for silicate weathering. Orange arrows represent the different weathering regimes as indicated by the $\delta^{7}Li$, black crosses are indication when changes in weathering regime occurs. **C.** Reconstructed pCO_2 (ppm) using boron-based pH and alkalinity from Caves et al. (2016), colored is indicating the site (filled light blue=806, filled dark blue=807), symbols represent the species (circle=*T. sacculifer* and triangle=*G. ruber*), filled grey squares (compilation A) are recalculated data based on Sosdian et al. (2018) at site 872. Data for compilation A are from: Hönisch and Hemming, 2009; Seki et al., 2010; Foster et al., 2012; Badger et al., 2013; Greenop et al., 2014; Martinez-Boti et al., 2015a; Chalk et al., 2017; Sosdian et al., 2018. Propagated uncertainties are given by eq. S17 for the dark blue envelope, while the light blue envelope are the uncertainties calculated based on eq. S16 (taking into account uncertainty on $\delta^{11}B_{seawater}$). Also shown are timing of major events. The rose band and dark rose band indicate eruption of the Columbia River flood basalts (Hooper et al., 2002) and time of maximum eruption (Kasbohm and Schoene, 2018), respectively.

Table 1: Core information.

Cruise	Leg	Hole	N (°)	E (°)	Depth (m)
ODP	130	807	3.61	156.62	2804
ODP	130	806	0.32	159.37	2520

Table 2: Comparison of reconstructed pCO_2 values for key intervals in the last 16 Myr.

Mid-Pleistocene transition (1.2-0.8 Ma)

MIS (G)	pCO_2 (ppm)	Reference	MIS (IG	pCO_2 (ppm)	Reference	pCO_2 amplitude IG-G (ppm)
20	179	This study	**21**	254	This study	75
22	187	This study	**23**	230	This study	43
24	*nd*		**25**	298	This study	*nd*
26	*nd*	This study	**27**	*nd*		*nd*
28	174	This study	**29**	*nd*		*nd*
30	170	This study	**31**	295	Hönisch et al., 2009 (N-TIMS)	125
32	218	Chalk et al., 2017	**33**	323	Chalk et al., 2017	105
34	197	Chalk et al., 2017	**35**	315	Chalk et al., 2017	118
36	189	Chalk et al., 2017	**37**	295	This study, Chalk et al., 2017	106
			39	306	This study	*nd*

Middle Pliocene Warm Period (3.29-2.97 Ma)

pCO_2 (ppm)	Reference
530 ± 110	This study (2 SD, n=4)
320 ± 130	Martinez-Boti et al., 2015b (2 SD, n=8)
360 ± 85	de la Vega et al., 2020 (2 SD, n=59)

Early Pliocene Warm Period (4.7-4.5 Ma)

pCO_2 (ppm)	Reference
419 ± 119	This study (2 SD, n=3)

Miocene Climate Optimum (17-14 Ma)

pCO_2 (ppm)	Reference
511 ± 201	This study (2 SD, n=3)
350-400	Foster et al., 2012
300-500	Greenop et al., 2014
470-630	Sosdian et al., 2018
687 ± 421	Rae et al., 2021 (2 SD, n=58)

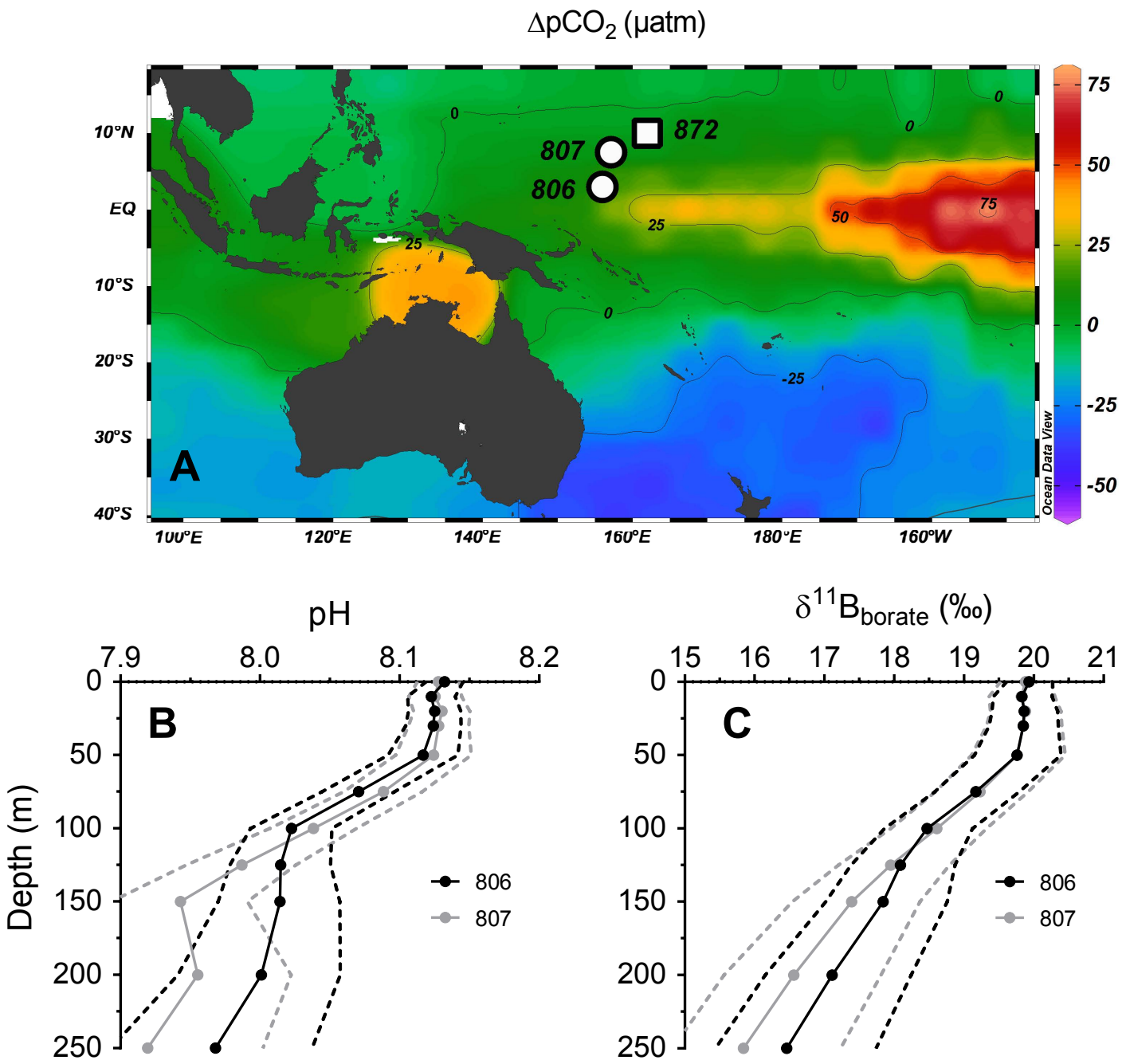
ΔpCO2 (μatm)
10°N
EQ
10°S
20°S
30°S
40°S
100°E
120°E
140°E
160°E
180°E
160°W
807
806
872
A
75
50
25
0
-25
-50
Ocean Data View
pH
7.9
8.0
8.1
8.2
B
Depth (m)
0
50
100
150
200
250
806
807
δ11Bborate (‰)
15
16
17
18
19
20
21
C

Figure 1

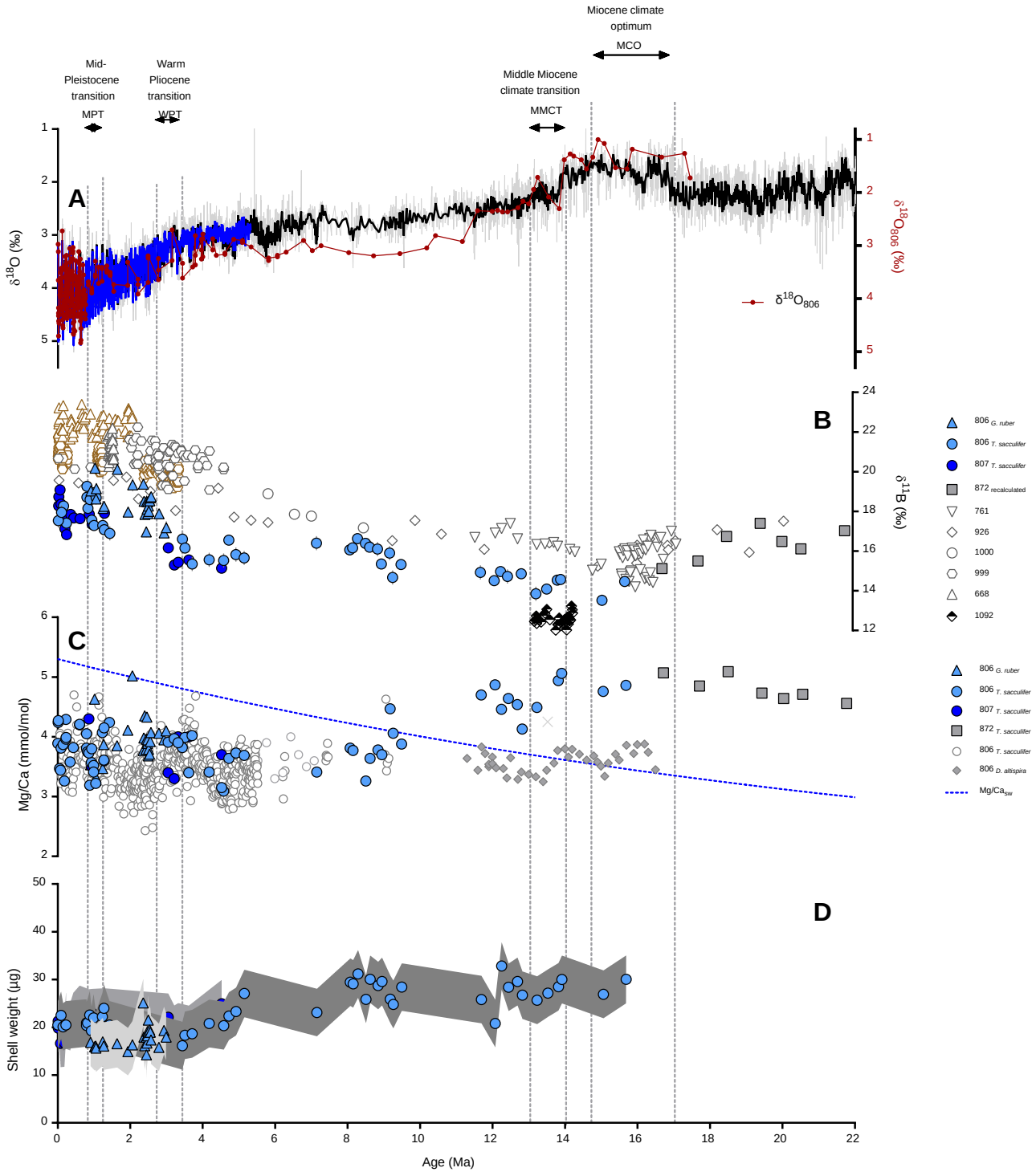
Miocene climate optimum
MCO
Mid-Pleistocene transition
MPT
Warm Pliocene transition
WPT
Middle Miocene climate transition
MMCT
A
B
C
D
δ18O (‰)
δ18O806 (‰)
δ18O806
δ11B (‰)
Mg/Ca (mmol/mol)
Shell weight (µg)
Age (Ma)
806 G. ruber
806 T. sacculifer
807 T. sacculifer
872 recalculated
761
926
1000
999
668
1092
872 T. sacculifer
806 D. altispira
Mg/Casw

Figure 2

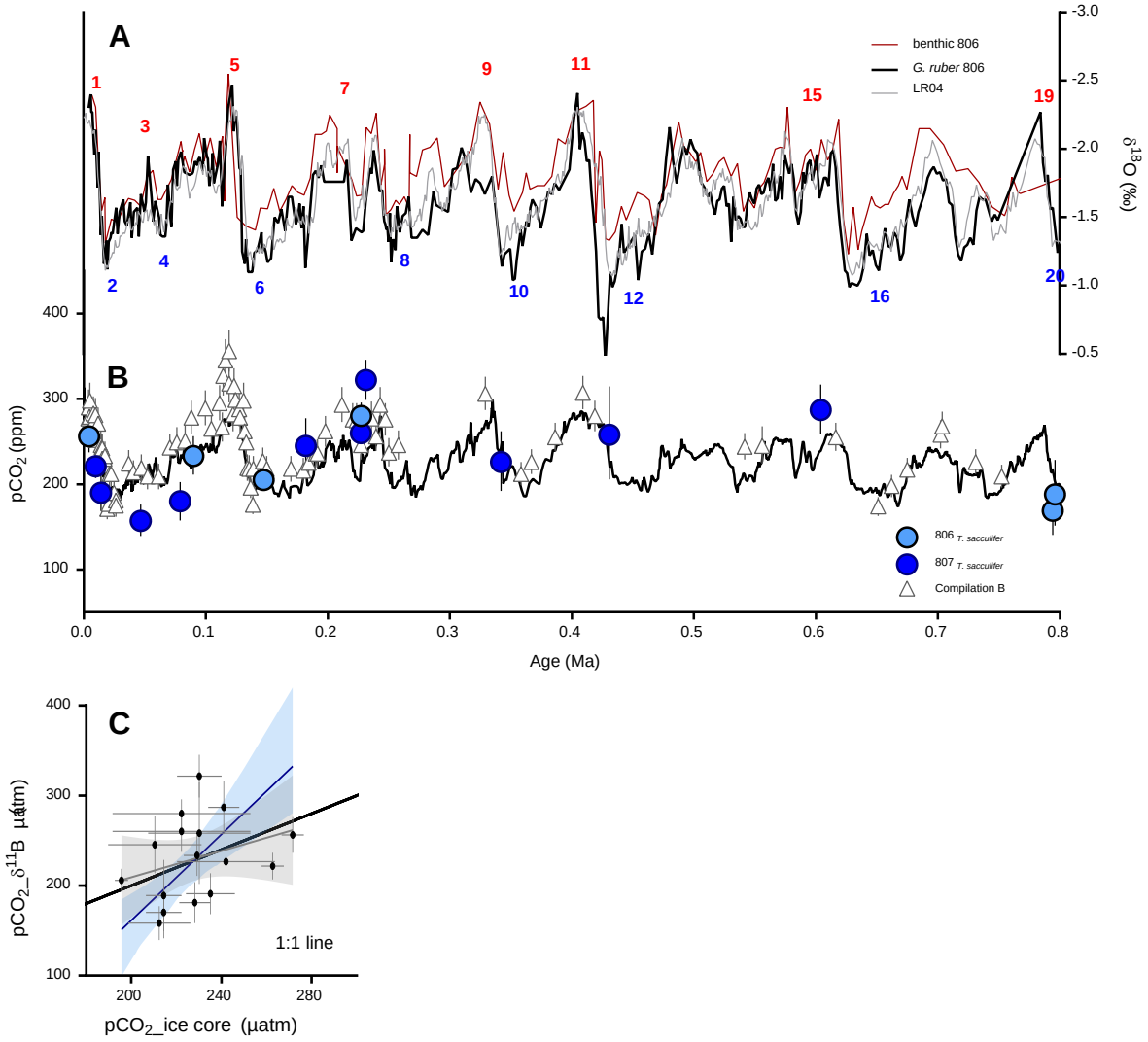
A
B
C
benthic 806
G. ruber 806
LR04
806 T. sacculifer
807 T. sacculifer
Compilation B
pCO2 (ppm)
δ18O (‰)
Age (Ma)
1:1 line
pCO2_δ11B (µatm)
pCO2_ice core (µatm)

Figure 3

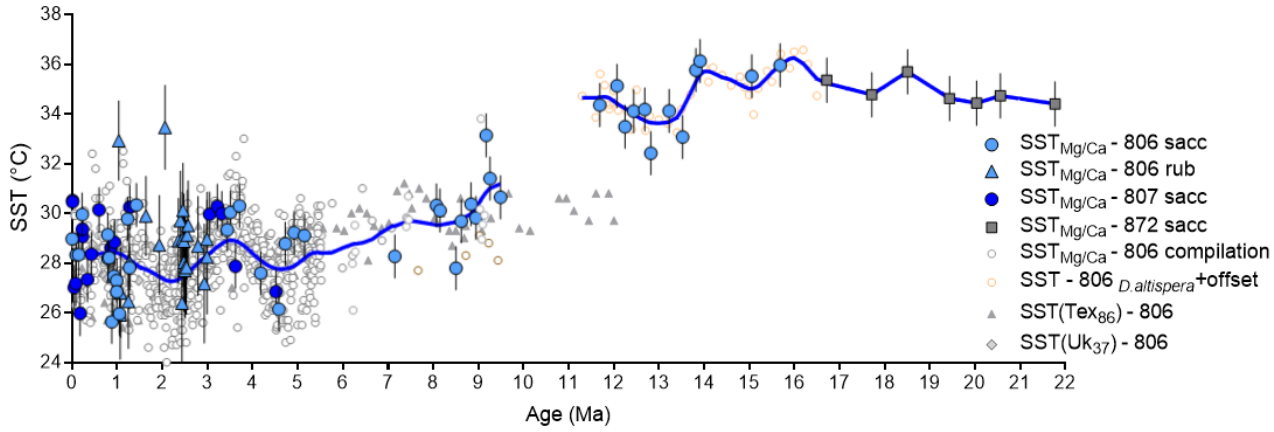
SST (°C)
Age (Ma)
SST$_{Mg/Ca}$ - 806 sacc
SST$_{Mg/Ca}$ - 806 rub
SST$_{Mg/Ca}$ - 807 sacc
SST$_{Mg/Ca}$ - 872 sacc
SST$_{Mg/Ca}$ - 806 compilation
SST - 806 $_{D.altispera}$+offset
SST(Tex$_{86}$) - 806
SST(Uk$_{37}$) - 806

Figure 4

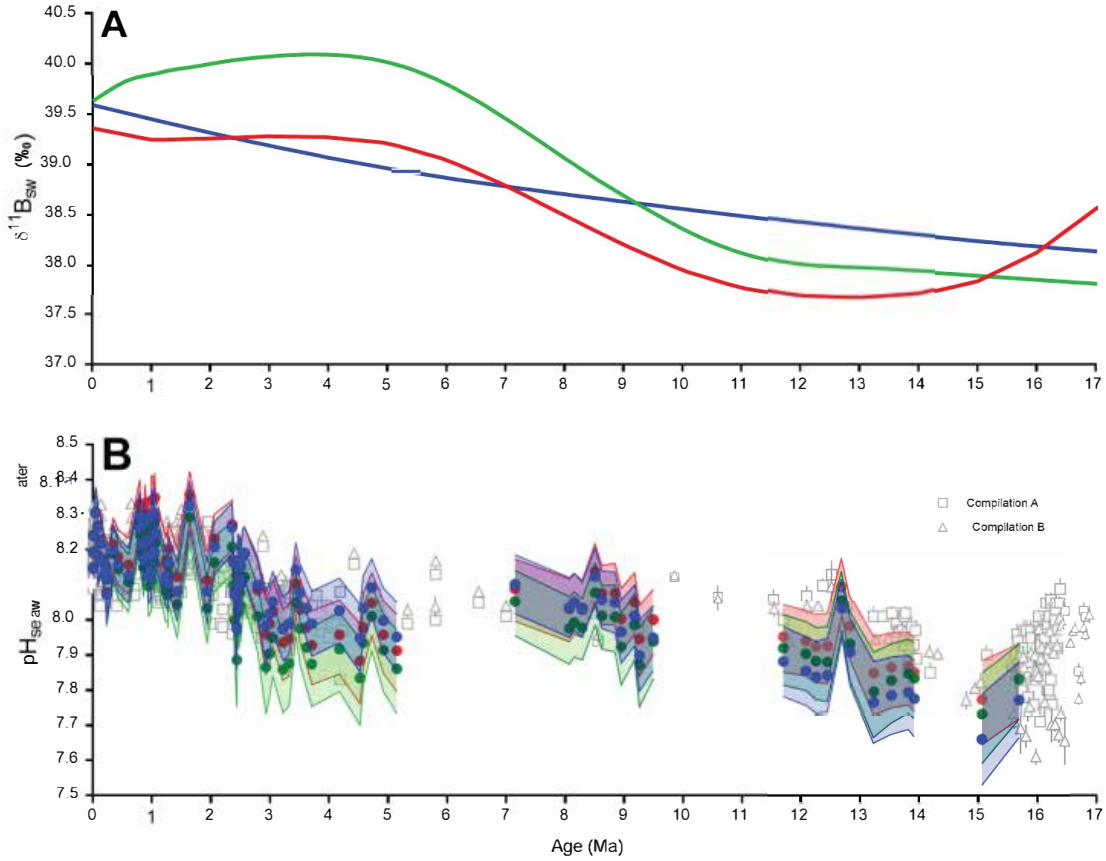

Figure 5

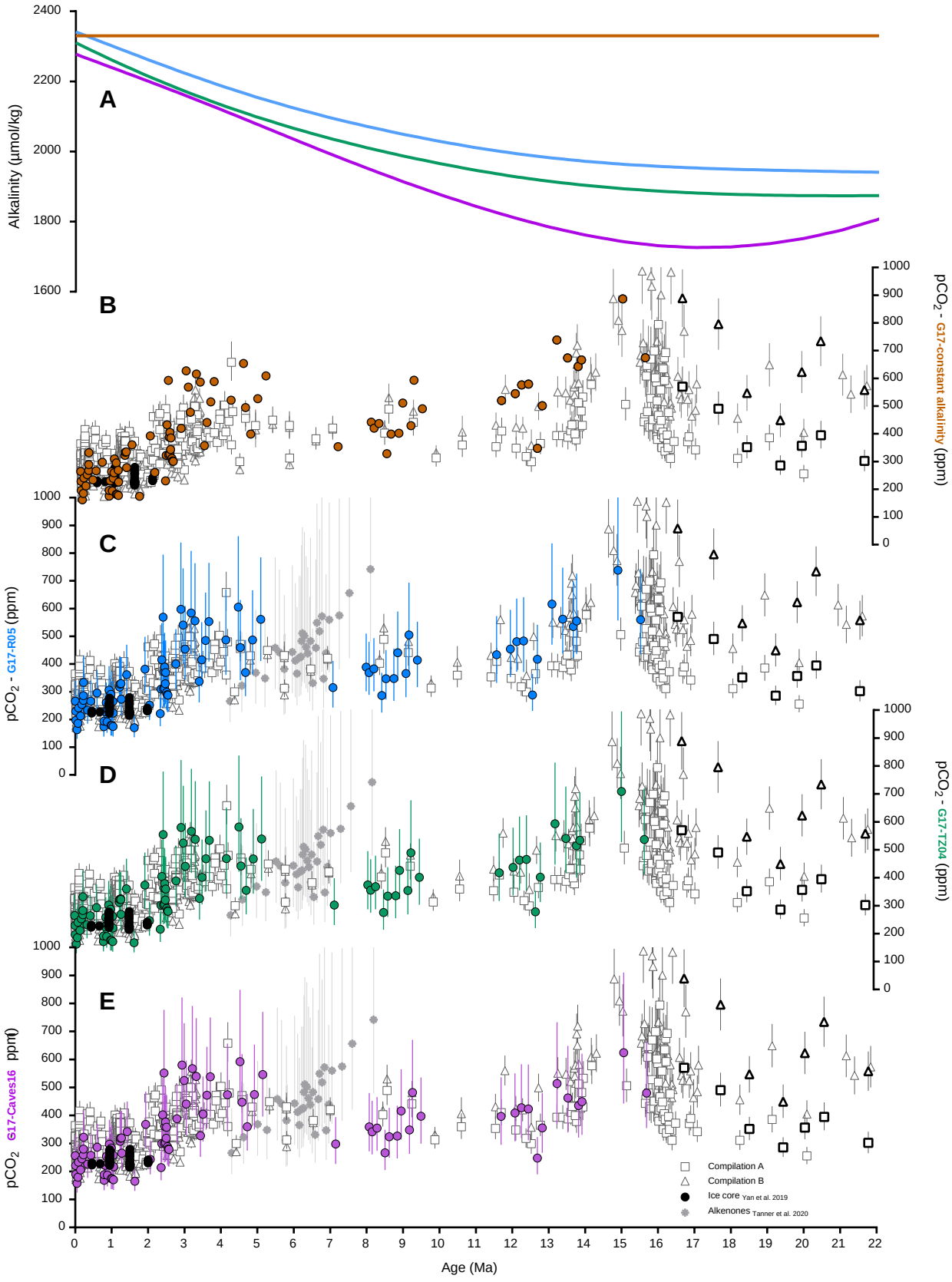
A
B
C
D
E
Alkalinity (µmol/kg)
pCO2 - G17-constant alkalinity (ppm)
pCO2 - G17-R05 (ppm)
pCO2 - G17-TZ04 (ppm)
pCO2 - G17-Caves16 (ppm)
Compilation A
Compilation B
Ice core Yan et al. 2019
Alkenones Tanner et al. 2020
Age (Ma)

Figure 6

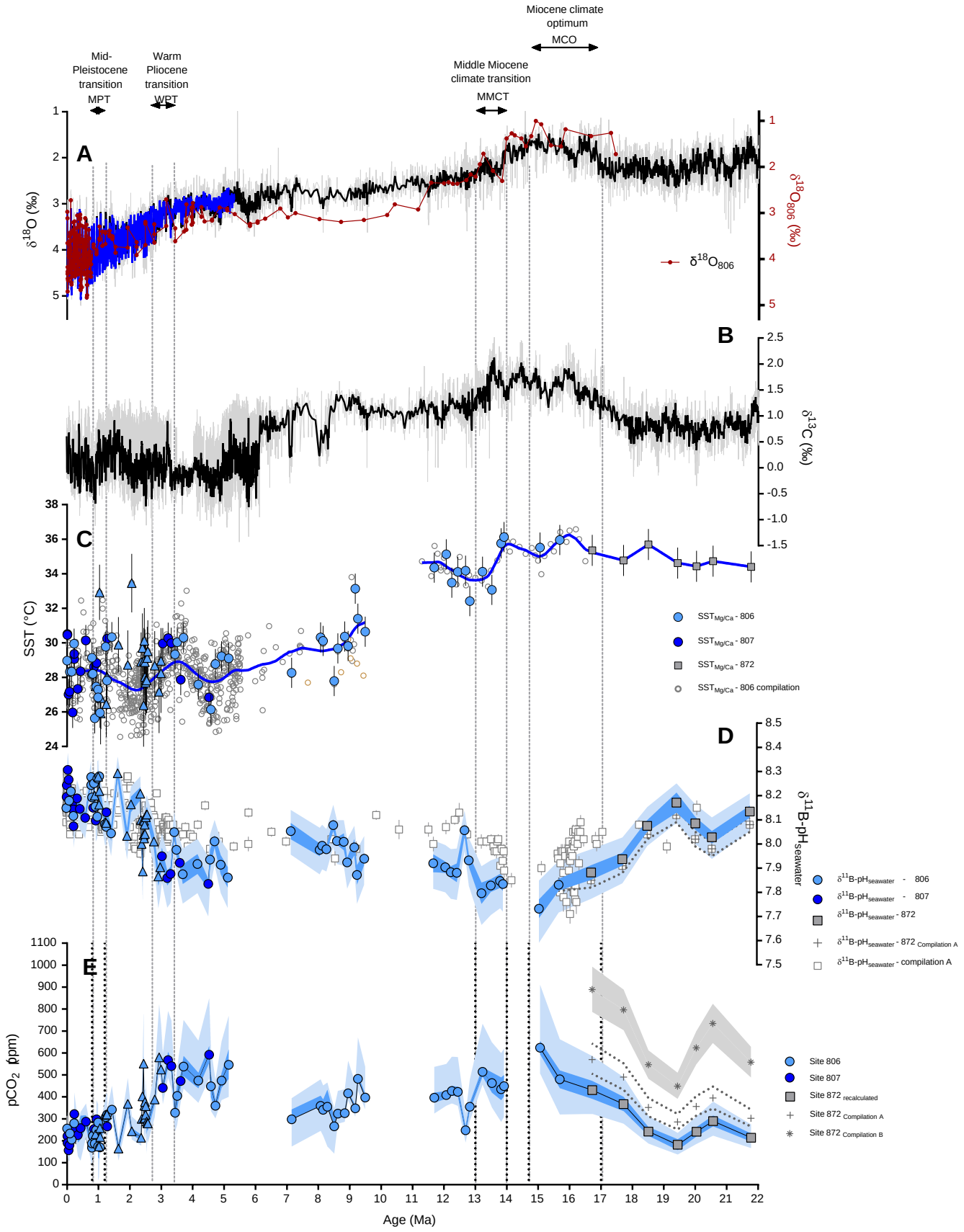
Miocene climate optimum
MCO
Mid-Pleistocene transition
MPT
Warm Pliocene transition
WPT
Middle Miocene climate transition
MMCT
A
B
C
D
E
δ18O (‰)
δ18O806 (‰)
δ18O806
δ13C (‰)
SST (°C)
SSTMg/Ca - 806
SSTMg/Ca - 807
SSTMg/Ca - 872
SSTMg/Ca - 806 compilation
δ11B-pHseawater
δ11B-pHseawater - 806
δ11B-pHseawater - 807
δ11B-pHseawater - 872
δ11B-pHseawater - 872 Compilation A
δ11B-pHseawater - compilation A
pCO2 (ppm)
Site 806
Site 807
Site 872 recalculated
Site 872 Compilation A
Site 872 Compilation B
Age (Ma)

Figure 7

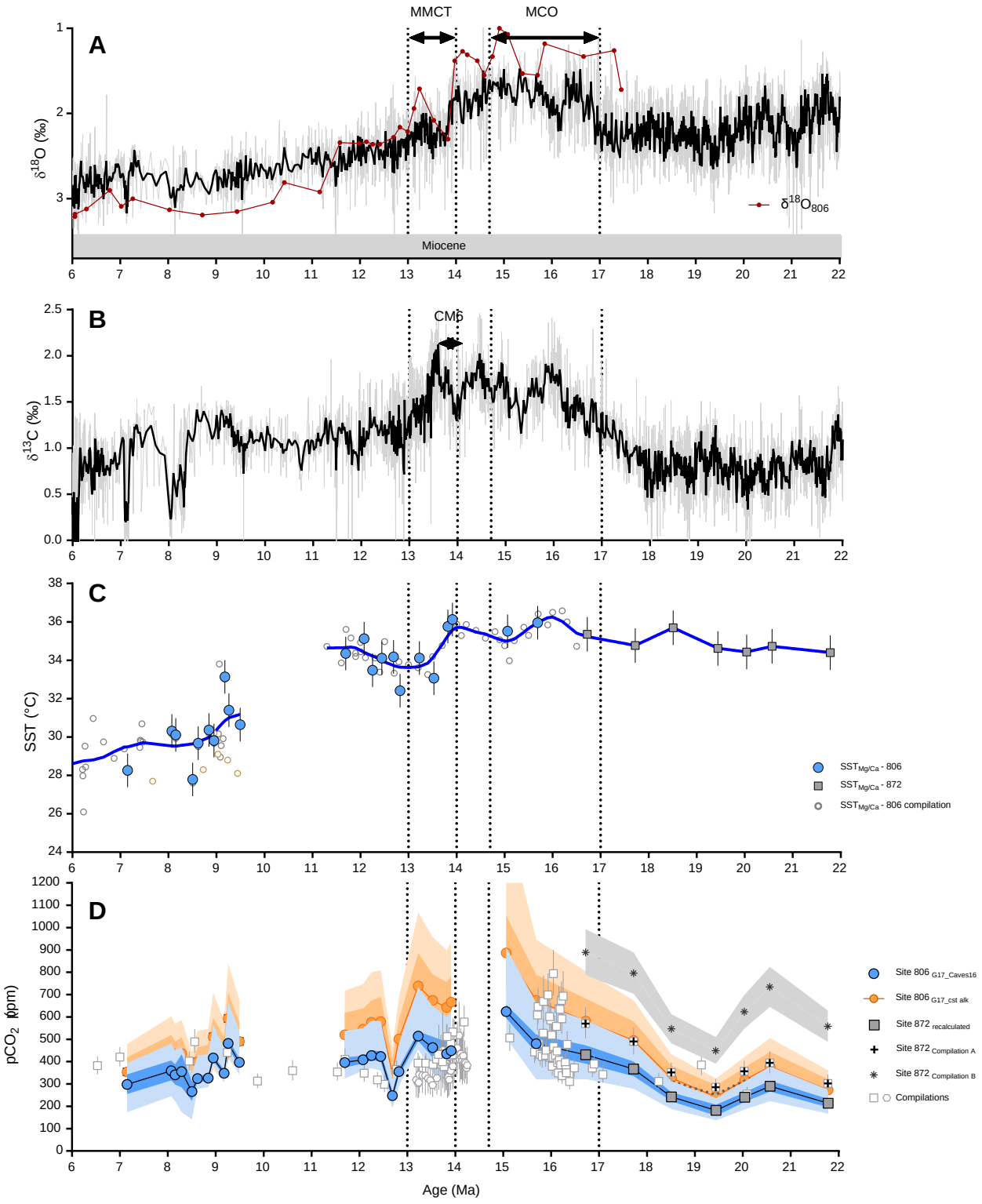
A
MMCT
MCO
δ18O (‰)
δ18O806
Miocene
B
CM6
δ13C (‰)
C
SST (°C)
SSTMg/Ca - 806
SSTMg/Ca - 872
SSTMg/Ca - 806 compilation
D
pCO2 (ppm)
Site 806 G17_Caves16
Site 806 G17_cst alk
Site 872 recalculated
Site 872 Compilation A
Site 872 Compilation B
Compilations
Age (Ma)

Figure 8

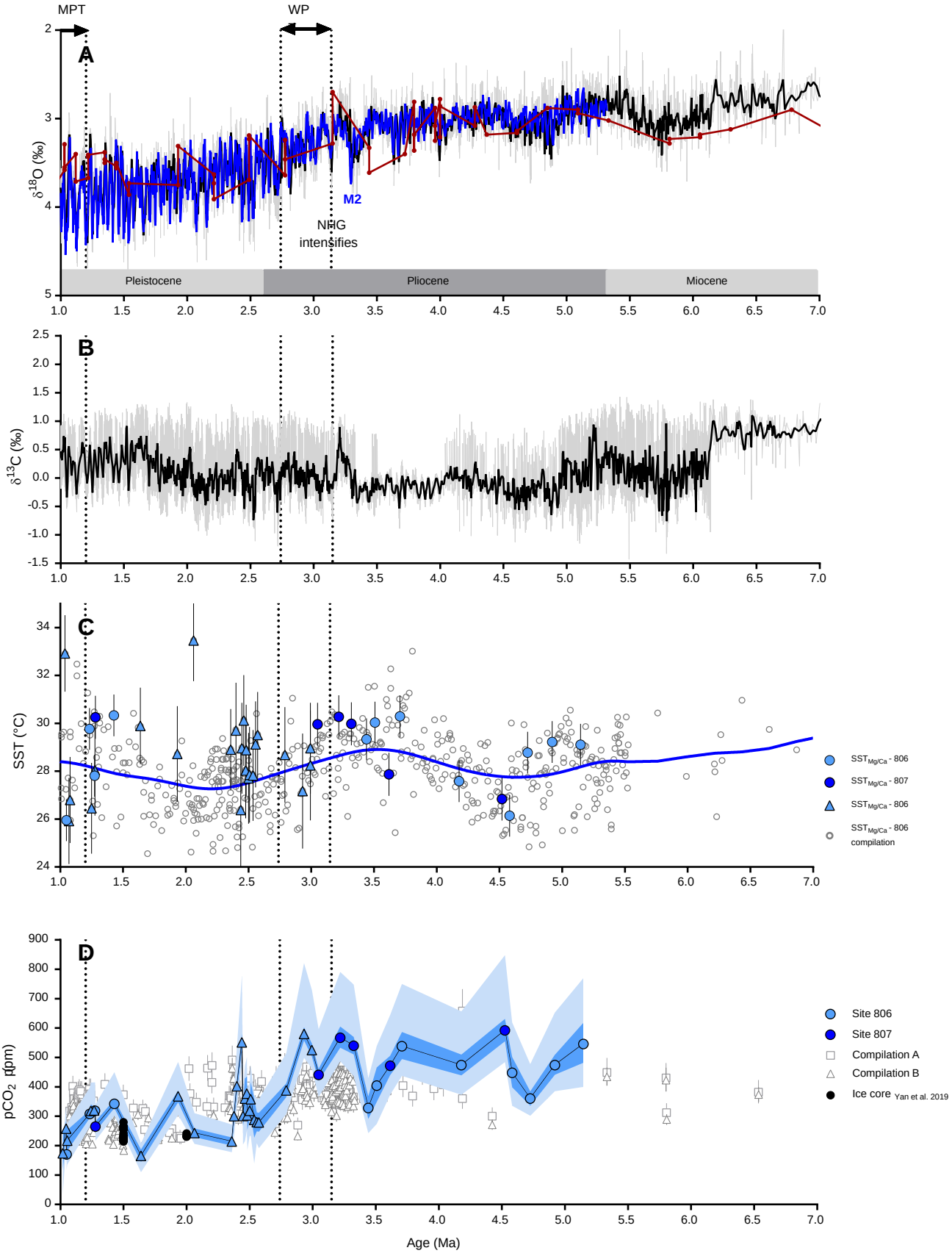
MPT
WP
A
M2
NHG intensifies
Pleistocene
Pliocene
Miocene
δ18O (‰)
B
δ13C (‰)
C
SST (°C)
SST Mg/Ca - 806
SST Mg/Ca - 807
SST Mg/Ca - 806
SST Mg/Ca - 806 compilation
D
pCO2 (ppm)
Site 806
Site 807
Compilation A
Compilation B
Ice core Yan et al. 2019
Age (Ma)

Figure 9

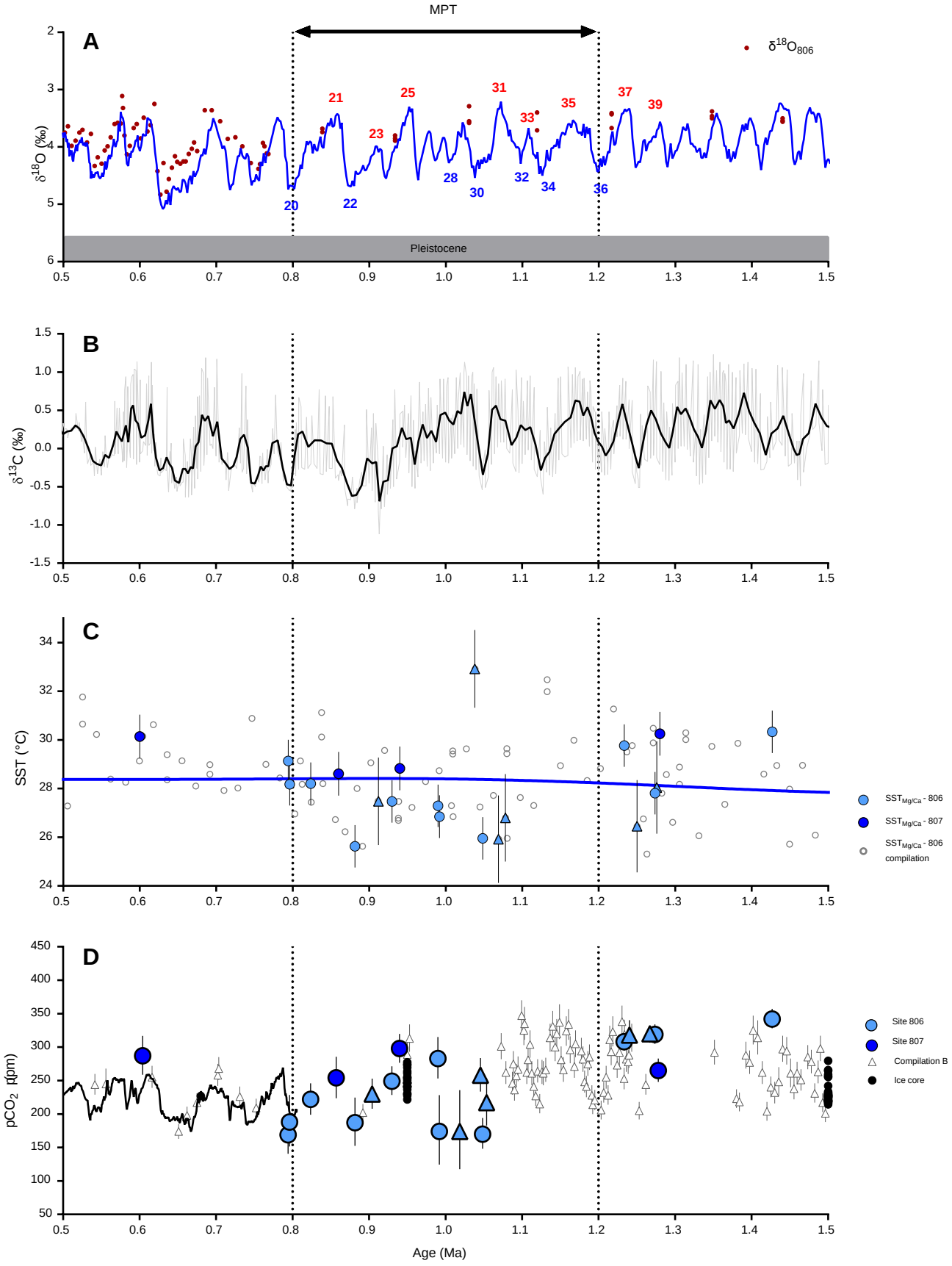
MPT
A
$\delta^{18}O_{806}$
$\delta^{18}O$ (‰)
Pleistocene
20
21
22
23
25
28
30
31
32
33
34
35
36
37
39
B
$\delta^{13}C$ (‰)
C
SST (°C)
$SST_{Mg/Ca}$ - 806
$SST_{Mg/Ca}$ - 807
$SST_{Mg/Ca}$ - 806 compilation
D
pCO_2 (ppm)
Site 806
Site 807
Compilation B
Ice core
Age (Ma)

Figure 10

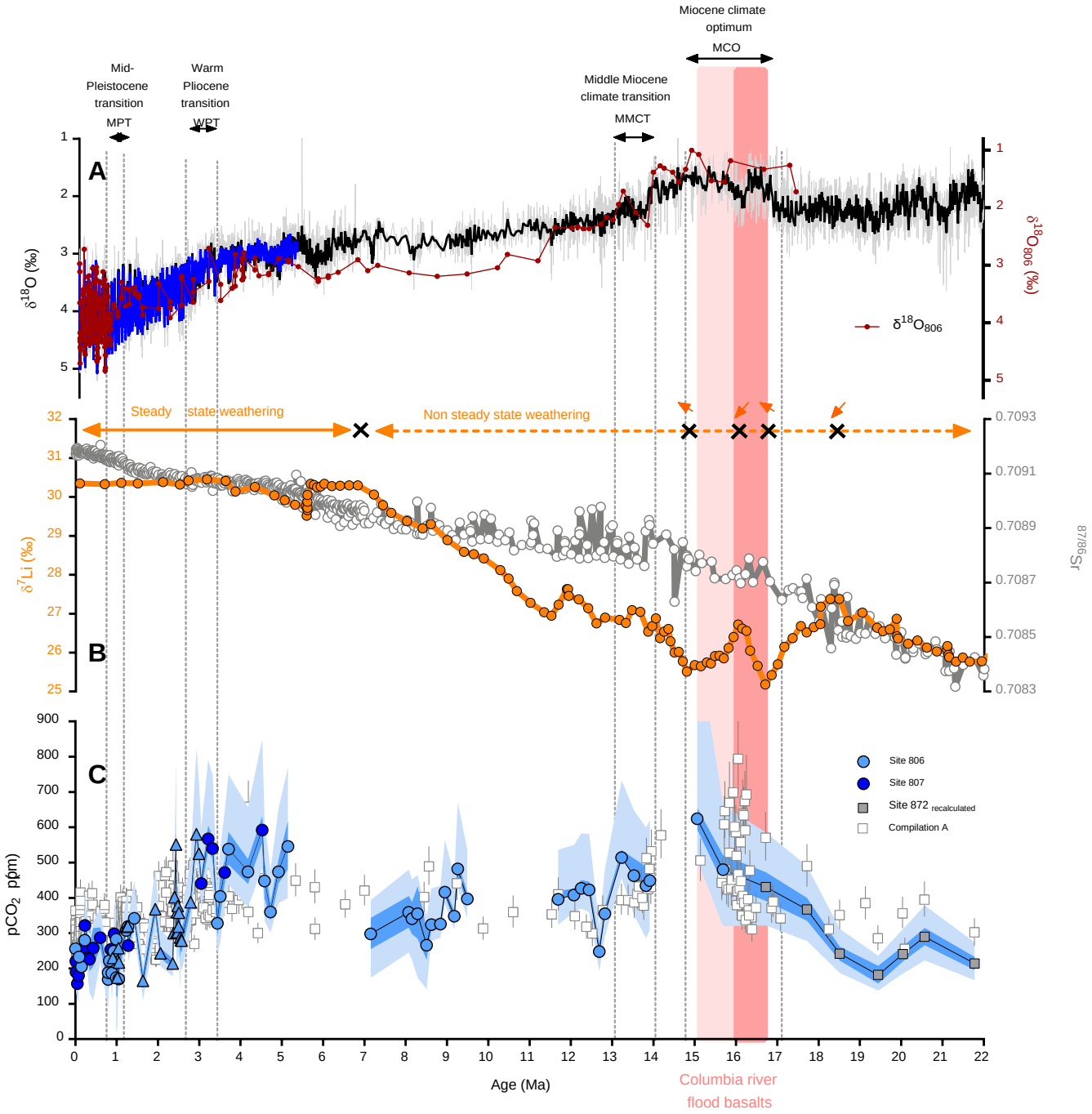
Miocene climate optimum
MCO
Mid-Pleistocene transition
MPT
Warm Pliocene transition
WPT
Middle Miocene climate transition
MMCT
A
δ18O (‰)
δ18O806 (‰)
δ18O806
Steady state weathering
Non steady state weathering
B
δ7Li (‰)
87/86Sr
C
pCO2 (ppm)
Site 806
Site 807
Site 872 recalculated
Compilation A
Age (Ma)
Columbia river flood basalts

Figure 11